

A flexible traffic stream model and its three representations of traffic flow



Liang Zheng^a, Zhengbing He^{b,*}, Tian He^c

^a School of Traffic and Transportation Engineering, Central South University, Changsha, China

^b MOE Key Laboratory for Urban Transportation Complex Systems Theory and Technology, Beijing Jiaotong University, Beijing, China

^c College of Resource and Environmental Science, Hunan Normal University, Changsha, China

ARTICLE INFO

Article history:

Received 13 September 2016

Received in revised form 22 November 2016

Accepted 14 December 2016

Available online 27 December 2016

Keywords:

Traffic stream model

Car-following model

Fundamental diagram

Lagrangian coordinate

ABSTRACT

To connect microscopic driving behaviors with the macro-correspondence (i.e., the fundamental diagram), this study proposes a flexible traffic stream model, which is derived from a novel car-following model under steady-state conditions. Its four driving behavior-related parameters, i.e., reaction time, calmness parameter, speed- and spacing-related sensitivities, have an apparent effect in shaping the fundamental diagram. Its boundary conditions and homogenous case are also analyzed in detail and compared with other two models (i.e., Longitudinal Control Model and Intelligent Driver Model). Especially, these model formulations and properties under Lagrangian coordinates provide a new perspective to revisit the traffic flow and complement with those under Eulerian coordinate. One calibration methodology that incorporates the monkey algorithm with dynamic adaptation is employed to calibrate this model, based on real-field data from a wide range of locations. Results show that this model exhibits the well flexibility to fit these traffic data and performs better than other nine models. Finally, a concrete example of transportation application is designed, in which the impact of three critical parameters on vehicle trajectories and shock waves with three representations (i.e., respectively defined in $x-t$, $n-t$ and $x-n$ coordinates) is tested, and macro- and micro-solutions on shock waves well agree with each other. In summary, this traffic stream model with the advantages of flexibility and efficiency has the good potential in level of service analysis and transportation planning.

© 2016 Elsevier Ltd. All rights reserved.

1. Introduction

In the field of traffic flow theory, it is always desirable to bridge microscopic car-following (CF) behaviors and macroscopic traffic flow. A simple yet flexible traffic flow model, which not only describes vehicle longitudinal operational control satisfactorily under various scenarios, but also characterizes the basic relationships between macro-traffic variables, is the interest for world-wide researchers. Usually, the relations between macro-traffic variables can be presented as continuum traffic flow models or fundamental diagrams. As for the connection between CF rules and corresponding macroscopic traffic flow models, a large number of related researches can be traced. Berg et al. (2000) developed a continuum model from the optimal velocity model using a series expansion of headway in terms of the density, which enables predictions of global impact and characteristics of any car-following model using the analogous continuum model. Later, Gupta and Katiyar

* Corresponding author.

E-mail addresses: zhengliang@csu.edu.cn (L. Zheng), he.zb@hotmail.com (Z. He).

(2006) employed this series expansion method to derive a new anisotropic continuum model based upon an improved car-following model and obtained some important and realistic model properties. On the other hand, Lee et al. (2001) presented a coarse-graining procedure to derive macroscopic fluid-dynamic models from microscopic car-following models, and took the optimal velocity model as an example for demonstration, in which properties of macro- and micro-models have a reasonable agreement. Specially, this derivation method can be extended to general car-following models. Zhou and Lü (2011) also utilized this coarse graining method to develop a macroscopic model from the generalized optimal velocity model. Besides, Zhang (2002) derived an anisotropic continuum model from a GM (General Motors) car-following model (Chandler et al., 1958), with the transformation method between micro- and macro-variables proposed by Liu et al. (1998). Jiang et al. (2002) applied the same transformation method to obtain an anisotropic continuum model from fully velocity difference (FVD) model (Jiang et al., 2001). Afterwards, Tang et al. (2009) also utilized this transformation method to put forward a new dynamic model for heterogeneous traffic flow consisting of buses and cars from a vehicle type-dependent heterogeneous car-following model. Zheng et al. (2015) employed this method to get an anisotropic continuum model, considering bi-directional information impact from a bi-directional car-following model based on Helly's framework (Helly, 1959). What attracts our attention is that Helbing (2009) compared several different approaches allowing one to derive macroscopic traffic equations directly from microscopic car-following models. Those approaches included a gradient expansion approach, a linear interpolation approach and an approach reminding of smoothed particle hydrodynamics.

On the other hand, fundamental relations of traffic flow have been established either empirically or derived from car-following models. Early derivations of the fundamental diagrams from car-following were carried out in order to study the aggregate-level behavior of proposed car-following rules and validate such rules against real-world data (e.g., Edie, 1963; Gazis et al., 1959; Newell, 1961; Pipes, 1965). It was not long, however, before the fundamental diagram induced by car-following theory itself began to attract the interest (Pipes, 1967). Later, Treiber et al. (2000) put forward the well-known intelligent driver model (IDM) and gave out the macro-correspondence under steady-state conditions, i.e., speed-gap equilibrium relation, which help understand the traffic phenomena and their correlation with car-following rules. Zhang and Kim (2005) proposed car-following rules that result in the fundamental diagrams with capacity drops and hysteresis loops; empirical investigation was carried out in Kim and Zhang (2004). Furthermore, Kim and Zhang (2008) demonstrated how heterogeneity in the driver population alone can be used to explain the observed scatter in flow-density plots. Rakha and Arafah (2010) carried out the transformation between Van Aerde's car-following model (i.e., Van Aerde, 1995) and the macro-correspondence (i.e., speed-density relationship), and utilized a heuristic automated tool named SPD_CAL to calibrate them using loop detector data. Jabari et al. (2014) presented the derivation of probabilistic stationary speed-density relation from Newell's simplified car-following model, whose probabilistic nature allows for investigating the impact of driver heterogeneity on the heavy scatter in flow-density data in congested traffic. Recently, Ni et al. (2015) proposed a longitudinal control model (LCM) and derived the corresponding traffic stream model under steady-state conditions, which had good capability of fitting empirical traffic data. LCM was also proved to be consistent at the microscopic and macroscopic levels.

This work attempts to put forward a traffic stream model with an excellent flexibility, even better than LCM. In LCM, its flexibility mainly depends on the calmness parameter, which is defined in an emergency and related to the emergency decelerations of two successive vehicles. However, driving behavior-related parameters that play an important role in normal driving regimes (e.g., free flow, approaching, stopping, etc.) would also influence the macroscopic traffic behaviors. Intuitively, the driver's sensitivity to speed- and spacing-related traffic information would definitely influence his/her operations in both normal and emergency situations (c.f., IDM), which aggregately makes the fundamental diagrams exhibit various shapes. Therefore, a novel car-following model, that incorporates the reaction time, calmness parameter, speed- and spacing-related sensitivities, will be proposed to describe the vehicle longitudinal motion. Obviously, it inherits the advantages LCM and IDM, and is more flexible and general. Then, its macro-correspondence will be derived to include these four critical driving behavior-related parameters, which help guarantee the excellent flexibility. Because of the micro-macro coupling relationship, i.e., the microscopic equation to its macroscopic equivalent, the macroscopic traffic behavior illustrated by the fundamental diagram can be explained or predicted by traffic flow modeling and simulation based on the microscopic CF model.

Traditional fundamental diagrams (i.e., flux-speed-density relations) are usually developed based on the spatial-temporal ($x-t$) coordinate, i.e., Eulerian coordinate, and corresponding traffic variables are measured by fixed-point detectors, e.g., inductive loop detectors. Lagrangian coordinate n , in hydrodynamics, is a physical coordinate that moves along with the flow and can be considered as the continuous version of accumulative number of vehicles (ANV) in traffic flow (Leclercq et al., 2007; Herrera and Bayen, 2010; Claudel and Bayen, 2010; Laval and Leclercq, 2013). The traffic states in Lagrangian coordinates can be detected by new vehicle detection technologies, e.g., GPS probe vehicle technologies, Video-Detection technologies, Automatic Vehicle Identification (AVI) technologies and Cellular probe vehicle technologies. To better understand micro- and macro-traffic phenomena from a completely new perspective, vehicular trajectories, macro-traffic variables and fundamental relations will be also defined in Lagrangian coordinates (i.e., $n-t$ and $x-n$ coordinates). From the micro-perspective, the vehicular trajectory can be inspected and defined from three possible 2-dimensional coordinate systems (Makigami et al., 1971; Jin and Ran, 2011), i.e., Eulerian coordinate $x-t$, and Lagrangian coordinates $n-t$ and $x-n$. These three kinds of vehicular trajectory provide completely various physical meanings for vehicular flow and correspond to different ways of traffic data detection aforementioned (Jin and Ran, 2011). Meanwhile, at the macro-aspect, the fundamental relation (in $x-t$ coordinate) can also be re-formulated with traffic variables defined in Lagrangian coordinates, based on which LWR

model (Lighthill and Whitham, 1955; Richards, 1956) with three representations can be presented to describe the traffic flow dynamics from three various viewpoints. Especially, Laval and Leclercq (2013) completed the theory framework of Hamilton-Jacobi partial differential equations to LWR model under $x-t$, $n-t$ and $x-n$ coordinates, and showed explicit solution methods and examples for the triangular flow-density diagram.

In this study, three representations of traffic flow (i.e., with micro- and macro-traffic variables and fundamental relations respectively defined on $x-t$, $n-t$ and $x-n$ coordinates) will be described and compared. The rest of the paper is organized as the following: Section 2 presents the derivation of a flexible traffic stream model (abbreviated as FTSM) from a car-following model under steady-state conditions, which can represent various shapes of fundamental relations. Section 3 analyzes the model properties and compares with other two models. Calibration of FTSM based on loop/microwave detector data from a wide range of facilities is carried out in Section 4. An example of FTSM's application is elaborated in Section 5. Finally, some important findings are concluded in Section 6.

2. The flexible traffic stream model

Macroscopic traffic phenomena can be treated as the exhibition of aggregated micro-driving behaviors. In order to dig the potential relation between the interaction of inter-drivers and fundamental diagrams presented, one alternative way is to directly build macroscopic steady-state models (i.e., fundamental relations between macro-variables) from microscopic car-following models. Therefore, a simple, physically meaningful and consistent traffic model is desirable. This section will introduce such a flexible traffic stream model with three representations, which is derived from one novel car-following model.

2.1. A novel car-following model

Inspired by the model framework of IDM and LCM, a new car-following model is formulated as

$$\ddot{x}_i(t + \tau_i) = A_i \left\{ 1 - \left[\frac{\dot{x}_i(t)}{v_i} \right]^\delta - \left[\frac{s_{ij}^*(t)}{s_{ij}(t)} \right]^\sigma \right\} \quad (1)$$

where τ_i is the reaction time of driver i , v_i is the desired speed of driver i , \dot{x}_i is the speed of driver i , A_i is the maximum acceleration desired by driver i when starting from standing still, $s_{ij}(t)$ is the actual spacing between vehicle i and its leading vehicle j (include the vehicle length), s_{ij}^* is the desired value of $s_{ij}(t)$, δ and σ respectively denote the driver's sensitivity coefficients about velocity and spacing information ($\delta > 0$ and $\sigma > 0$).

Moreover, the desired spacing can be formulated based on the safety rule as

$$s_{ij}^*(t) = \frac{\dot{x}_i^2(t)}{2b_i} - \frac{\dot{x}_j^2(t)}{2B_j} + \dot{x}_i \tau_i + l_j \quad (2)$$

where $s_{ij}^*(t) \geq l_j$ and l_j is the vehicle j 's effective length (i.e., actual vehicle length plus some buffer spaces at both ends), B_j represents driver i 's estimate of the emergency deceleration most likely to be applied by driver j ($B_j > 0$), b_i can be interpreted as the deceleration which driver i believes that he or she is capable of applying in an emergency ($b_i > 0$). Furthermore, the driver i 's degree of calmness can be written as

$$r_i = \frac{1}{2} \left(\frac{1}{b_i} - \frac{1}{B_j} \right) \quad (3)$$

That is, the larger r_i means the driver is more calm.

This car-following model has a simple formulation but can describe a driver's stimulus-response mechanism effectively. That is, the driver adjusts his/her acceleration at the delay τ_i according to two ratios: one is the ratio between the current and desired speed; the other is between the current and expected spacing. Specifically, the driver tends to decelerate when faster than the desired speed or trapped in the dangerous spacing (i.e., smaller than the desired spacing), and vice versa. The sensitivities δ and σ respectively control the degree of response to speed- and spacing-related ratio information. More specifically, compared with IDM, the significant differences exist at the aspects of desired spacing, reaction time and spacing-related sensitivity. Moreover, Eq. (1) can also be apparently distinguished from LCM in terms of velocity-related sensitivity and reaction mechanism to the spacing information. Their detailed differences from the macroscopic viewpoint will be further discussed in Section 3.3.

Furthermore, it can be easily checked that this car-following model satisfies the consistency criteria proposed in Treiber and Kesting (2013), and the validation process can refer to Appendix A. That is also to say, Eq. (1) can consistently describe all situations that may arise in single-lane traffic, e.g., free flow, approaching, normal and emergency stoppings, etc., and is more comprehensive than simply car-following as it is conventionally termed.

2.2. Macroscopic correspondences in three coordinates

2.2.1. Background: Eulerian and Lagrangian definitions

To derive macroscopic counterparts of the car-following model (c.f., Eq. (1)) in Lagrangian (Vehicular) coordinates, vehicular trajectories and traffic variables defined in Lagrangian coordinates should be firstly introduced. Inspired by three-dimensional traffic flow surface provided by Makigami et al. (1971), vehicle trajectories can be re-defined in three coordinates as: Lagrangian (Vehicular) trajectory $x^n(t)$ corresponds to the trajectory of all vehicles located at the n th vehicle from the origin vehicle on the x - t diagram, which does not necessarily follow the trajectory of a physical vehicle i . In n - t diagram, trajectory $n^x(t)$ represents the relationship between time t and the number of vehicles arriving at x by time t ; and in x - n diagram, each trajectory is a “snapshot” of the location of each vehicle at time t . In all three coordinates, the vehicular coordinate increases over time but decreases over space, which leads to the negative signs in the following Eulerian and Lagrangian (Vehicular) definitions for traffic variables (Jin and Ran, 2011).

$$\begin{cases} k = -\frac{\partial n(x,t)}{\partial x}, & q = \frac{\partial n(x,t)}{\partial t} \\ s = -\frac{\partial x(n,t)}{\partial n}, & v = \frac{\partial x(n,t)}{\partial t} \\ h = \frac{\partial t(n,x)}{\partial x}, & p = \frac{\partial t(n,x)}{\partial n} \end{cases} \quad (4)$$

where k is traffic density, q traffic flux, v traffic space-mean speed, $s = 1/k$ the spacing between two vehicles, $h = 1/v$ the pace (or travel time over a unit distance) and $p = 1/q$ the time headway between two vehicles. Hence, the equilibrium fundamental relations in all three coordinates are formulated as

$$\begin{cases} q = Q_e(k) \\ v = V_e(s) \\ p = P_e(h) \end{cases} \quad (5)$$

Here, $Q_e(\cdot)$ is called Eulerian fundamental relation defined on x - t coordinate, while $V_e(\cdot)$ and $P_e(\cdot)$ are Lagrangian fundamental relations respectively defined on n - t and x - n coordinates.

2.2.2. Derivation of FTSM

Under steady-state conditions, that is, the acceleration in Eq. (1) is equal to zero, vehicles in traffic behave uniformly, and their identities can be dropped. Therefore, Eq. (1) can be aggregated to its macroscopic equivalent (i.e., FTSM) as

$$v = v_f [1 - (k/k^*)^\sigma]^{1/\delta} \quad (6)$$

where v_f free-flow speed, and k^* takes the following form

$$k^* = \frac{1}{s^*} = \frac{1}{r\nu^2 + \tau\nu + l} \quad (7)$$

where r and τ respectively denote the calmness parameter and average response time for driver population, and l denotes average effective vehicle length. Therefore, the traffic stream model in Eulerian coordinate (x - t) can be expressed as

$$k = (r\nu^2 + \tau\nu + l)^{-1} \left[1 - (\nu/v_f)^\delta \right]^{1/\sigma} \quad (8)$$

or

$$q = k\nu = \nu(r\nu^2 + \tau\nu + l)^{-1} \left[1 - (\nu/v_f)^\delta \right]^{1/\sigma} \quad (9)$$

Furthermore, its equivalents in Lagrangian coordinates are respectively written as

$$s = (r\nu^2 + \tau\nu + l)^{-1} \left[1 - (\nu/v_f)^\delta \right]^{-1/\sigma} \quad \text{in } n-t \text{ coordinate} \quad (10)$$

and

$$p = h \left(rh^{-2} + \tau h^{-1} + l \right)^{-1/\sigma} \left[1 - (h_f/h)^\delta \right]^{-1/\sigma} \quad \text{in } x-n \text{ coordinate} \quad (11)$$

where $h_f = 1/v_f$. The equilibrium relations (10) and (11) are also called Lagrangian fundamental relations.

3. Property analyses for FTSM

3.1. Boundary conditions

All three representations of FTSM have two clearly defined boundary conditions. In x - t and n - t coordinates, when density approaches zero $k \rightarrow 0$ (i.e., $s \rightarrow \infty$), traffic flux approaches zero $q \rightarrow 0$ (also $\nu \rightarrow v_f$); when density approaches jam density

$k \rightarrow k_j$ (i.e., $s \rightarrow l$), traffic flux approaches zero $q \rightarrow 0$ (also $v \rightarrow 0$). While in x - n coordinate, when pace approaches infinity $h \rightarrow \infty$, the time headway approaches infinity $p \rightarrow \infty$; when pace approaches h_f (i.e., $1/\nu_f$), the time headway also approaches infinity $p \rightarrow \infty$. Then, kinematic wave speed, wave flux and wave spacing when traffic is jammed (respectively defined in $(x-t)$, $(n-t)$ and $(x-n)$ coordinates) can be determined by calculating the first derivatives of flow q (speed ν , time headway p) with respect to density k (spacing s , pace h) and evaluating the result at $k = k_j$, $s = l$ and $h = \infty$ respectively.

Hence, as for the kinematic wave speed at jam density in x - t coordinate, according to Eq. (9), we have

$$\frac{dq}{dk} = \frac{d(k\nu)}{dk} = \nu + k \frac{d\nu}{dk} = \nu + \frac{1}{s} \cdot \frac{d\nu}{d(1/s)} = \nu - \frac{s}{ds/d\nu} = \nu - \frac{s}{s'} \quad (12)$$

$$s' = \frac{ds}{d\nu} = \frac{(2r\nu + \tau)}{\left[1 - (\nu/\nu_f)^\delta\right]^{1/\sigma}} + \frac{\delta(r\nu^2 + \tau\nu + l)(\nu/\nu_f)^{\delta-1}}{\sigma\nu_f \left[1 - (\nu/\nu_f)^\delta\right]^{1/\sigma+1}} \quad (13)$$

$$\frac{dq}{dk} = \nu - \frac{s}{s'} = \nu - \frac{(r\nu^2 + \tau\nu + l)\left[1 - (\nu/\nu_f)^\delta\right]^{1/\sigma}}{(2r\nu + \tau)\left[1 - (\nu/\nu_f)^\delta\right]^{1/\sigma} + \frac{\delta}{\sigma\nu_f}(r\nu^2 + \tau\nu + l)[1 - (\nu/\nu_f)^\delta]^{1/\sigma-1}(\nu/\nu_f)^{\delta-1}} \quad (14)$$

Therefore,

$$\omega_j = \frac{dq}{dk}\Big|_{k=k_j, \nu=0} = -\frac{l}{\tau} \quad (15)$$

On another note, based on Eq. (10), the wave flux at jam condition in n - t coordinate is written as

$$\frac{d\nu}{ds}\Big|_{s=l, \nu=0} = \left\{ \frac{(2r\nu + \tau)}{\left[1 - (\nu/\nu_f)^\delta\right]^{1/\sigma}} + \frac{\delta(r\nu^2 + \tau\nu + l)(\nu/\nu_f)^{\delta-1}}{\sigma\nu_f \left[1 - (\nu/\nu_f)^\delta\right]^{1/\sigma+1}} \right\}^{-1} \Big|_{s=l, \nu=0} = \frac{1}{\tau} \quad (16)$$

On third note, based on Eq. (11), the wave spacing at jam state in x - n coordinate is derived as

$$\frac{dh}{dp} = \frac{d(1/\nu)}{d(1/q)} = \frac{-1/\nu^2 d\nu}{-1/q^2 dq} = \frac{k^2}{dq/d\nu} = \frac{1}{s^2 dq/d\nu} \quad (17)$$

$$\frac{dq}{d\nu} = \frac{d(k\nu)}{d\nu} = k + \nu \frac{dk}{d\nu} = k + \nu \frac{d(1/s)}{d\nu} = \frac{1}{s} - \frac{\nu}{s^2} \frac{ds}{d\nu} \quad (18)$$

$$\frac{dh}{dp}\Big|_{p=\infty, s=l, \nu=0} = \frac{1}{s - \nu ds/d\nu}\Big|_{p=\infty, s=l, \nu=0} = \frac{1}{l}, \text{ that is, } \frac{dp}{dh}\Big|_{h=\infty, s=l, \nu=0} = l \quad (19)$$

Obviously, each representation of FTSM has its own coordinate system-dependent kinematic wave speed (flux or spacing) formulation. Physical meanings of kinematic wave speed, wave flux and wave spacing at jam condition are also completely different from each other and provide three alternative ways to revisit these kinematic waves. In x - t coordinate, the wave speed at jam density means the jam traffic is propagated backwards at the speed of l/τ . While the wave flux in n - t coordinate means that vehicles are trapped in jam traffic at a rate of one vehicle every τ seconds, and the kinematic wave spacing in x - n coordinate implies that there is one vehicle being caught by the jam traffic every l distance. Moreover, these boundary conditions (i.e., Eqs. (15), (16) and (19)) in fact are consistent with those in Laval and Leclercq (2013). This results from the fact that the limiting case of FTSM is equivalent to the triangular flow-density diagram (i.e., $m = 3$) by Laval and Leclercq (2013), which will be analyzed in detail in Section 3.3.

3.2. Model flexibility

According to previous studies on the real traffic data, the flux-density relation was verified to exhibit a skewed parabolic shape (i.e., desirable property of concavity), a triangular shape, and even a mirrored-lambda shape (i.e., including the convex section) (Ni et al., 2015). Therefore, an attractive property of a traffic stream model is its flexibility to represent various flux-density shapes. Fortunately, FTSM employs six parameters that allow sufficient flexibility to fit traffic data from a wide range of facilities, and its shape depends on the second derivative of flow with respect to density

$$\frac{d^2q}{dk^2} = \frac{d(v - s/s')}{dk} = \frac{d\nu}{dk} - \frac{d(s/s')}{dk} = \frac{-s^3 s''}{s^3} \quad (20)$$

where

$$s'' = \frac{2r}{\left[1 - (\nu/v_f)^\delta\right]^{1/\sigma}} + \frac{\delta(2r\nu + \tau)(\nu/v_f)^{\delta-1}}{\sigma v_f \left[1 - (\nu/v_f)^\delta\right]^{1/\sigma+1}} \\ + \frac{\delta}{\sigma v_f} \left\{ \frac{(\nu/v_f)^{\delta-1}[(2r\nu + \tau) + (\delta - 1)(r\nu + \tau + l/\nu)]}{\left[1 - (\nu/v_f)^\delta\right]^{1/\sigma+1}} + \frac{\delta(1/\sigma + 1)(r\nu^2 + \tau\nu + l)(v/v_f)^{2\delta-2}}{v_f \left[1 - (\nu/v_f)^\delta\right]^{1/\sigma+2}} \right\} \quad (21)$$

Note that s is always positive, so the flow-density shape is determined by the signs of s' and s'' . If s' and s'' are both positive, d^2q/dk^2 is negative and the shape of flow-density relation is concave. Otherwise, the flow-density relationship may consist of a combination of concave, straight and convex sections. Thus, by adjusting the parameters v_f , τ , r , l , δ and σ , it is possible to result in a parabolic shape, a triangular shape, and even a mirrored-lambda shape. Of course, the set of parameters that provide non-concave flow-density relations can also be identified easily.

Among above six parameters, v_f and l are usually restricted respectively by the designed speed limit and traffic composition. Other four parameters (i.e., τ , r , δ and σ) play a critical role in shaping the flux-density curve, which is illustrated as the following.

Fig. 1(a) illustrates that with the decrease of reaction time, the capacity and traffic flux in the congested regime increases, and the critical density is also right-shifted. This implies the more rapid response of driver results in the higher traffic flow, especially in the congested range. As the drivers become less calm, i.e., r decreases from 0 to -0.03 , the flux-density curves firstly exhibit a parabolic shape, then show nearly a triangular shape and finally take a mirrored-lambda shape (c.f., **Fig. 1(b)**). Interestingly, the less calm the drivers, the larger traffic flux is generated during the medium density range and the critical density is slightly right-shifted. However, this may cause more potential collision risks. Similarly, as the drivers become more sensitive to speed-related information, the flux-density curve shows a parabolic shape, then nearly a triangular shape and finally a slight mirrored-lambda shape (c.f., **Fig. 1(c)**). Moreover, the capacity and traffic flux in the medium density range increase and the critical density is left-shifted with the increase of δ . In **Fig. 1(d)**, as spacing-related sensitivity increases, the capacity and traffic flux in the medium density range also grow, and the critical density is left-shifted. Especially, the flux-density relation gradually transforms from a parabolic shape to nearly a triangular shape, and ultimately takes a slight mirrored-lambda shape (c.f., **Fig. 1(d)**), which is similar to the change trend influenced by δ . In summary, τ , r , δ and σ have a great impact on the shape of flux-density curve, which allow the sufficient flexibility to fit data from a wide range of facilities; see details in Section 4.

3.3. A homogeneous case and its comparison with IDM and LCM

3.3.1. Analyses for homogeneous case of FTSM

From the microscopic viewpoint, if driver i is not willing to take the risk of tailgating and all drivers carry out the homogeneous emergence brake, we have $r_i = 0$, i.e., $b_i = B_j$. In this condition, the speed-spacing relation (i.e., Eq. (10)) can be simplified as

$$s = (\tau\nu + l) \left[1 - (\nu/v_f)^\delta\right]^{-1/\sigma} \quad (22)$$

When $\delta \rightarrow \infty$ or $\sigma \rightarrow \infty$, Eq. (22) becomes $s = (\tau\nu + l)$, that is, $V_e(s) = (s - l)/\tau$ or $V_e(k) = (1/k - 1/k_j)/\tau$, where $l = 1/k_j$. Therefore, $Q_e(k) = (1 - k/k_j)/\tau$ is for congested traffic state because the equilibrium flux decreases as the density increases, and the kinematic wave speed $\omega_j = -l/\tau$. Meanwhile, based on Eqs. (6), (7) and $r = 0$, when $\delta \rightarrow \infty$ or $\sigma \rightarrow \infty$, we easily get $V_e(k) = v_f$ and $Q_e(k) = v_f k$ for free flow state. Overall, $Q_e(k) = \min[v_f k, (1 - k/k_j)/\tau]$, or $V_e(s) = \min[v_f, (s - l)/\tau]$. Thus, a remarkable property of FTSM is the fact that it yields a bilinear fundamental diagram under some particular conditions, which accords with the statement provided by Del Castillo (2012), that is, a flexible model for the flux-density curve should include the bilinear or triangular fundamental diagram as a particular limiting case. Interesting, the limiting case of FTSM is also consistent with the triangular flow-density diagram (i.e., $m = 3$) by Laval and Leclercq (2013), under which their wave speed (wave flow or wave spacing) values accord with each other.

Furthermore, based on Eq. (22), two other special cases can be written as the following.

(1) When $\delta = 1$ and $\sigma = 2$, we obtain

$$V_e(s)|_{\delta=1, \sigma=2} = \frac{-l}{\tau} + \frac{s^2}{2v_f\tau^2} \left(-1 + \sqrt{1 + \frac{4\tau l v_f + 4\tau^2 v_f^2}{s^2}} \right) \quad (23)$$

(2) When $\delta = 2$ and $\sigma = 2$, we get

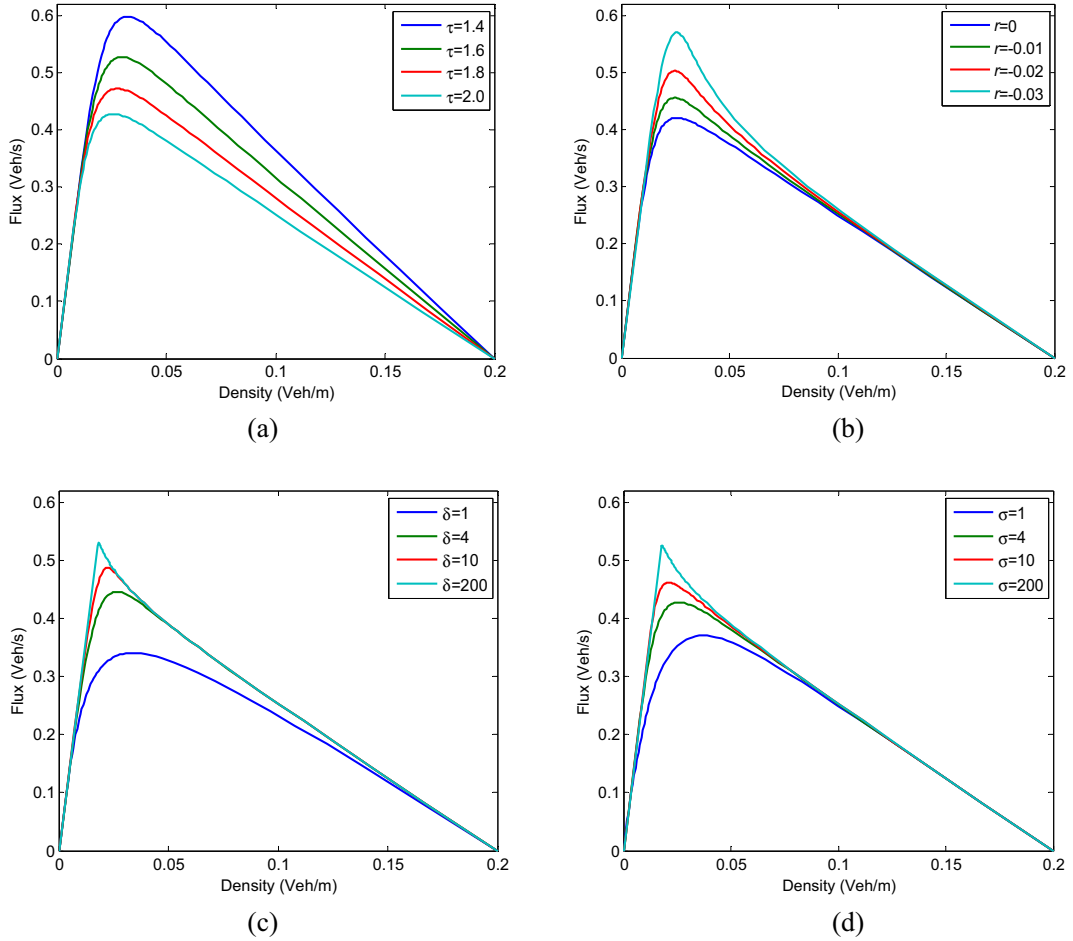


Fig. 1. Influence of four critical parameters on the shape of fundamental diagrams, $v_f = 30$ m/s and $k_j = 1/l = 0.2$ veh/m.

$$V_e(s)|_{\delta=2,\sigma=2} = \frac{-v_f^2}{(\tau^2 v_f^2 + s^2)} \left(\tau l - \sqrt{\tau^2 L^2 - \frac{(\tau^2 v_f^2 + s^2)(l^2 - s^2)}{v_f^2}} \right) \quad (24)$$

3.3.2. Related analyses for IDM

In order to compare FTSM with macro-correspondence of IDM (i.e., macro-IDM), IDM and its macroscopic counterpart are revisited here (Treiber et al., 2000). Firstly, IDM is formulated as

$$\ddot{x}_i(t) = A_i \left\{ 1 - \left[\frac{\dot{x}_i(t)}{v_i} \right]^\delta - \left[\frac{g_{ij}^*(t)}{g_{ij}(t)} \right]^2 \right\} \quad (25)$$

where $g_{ij}^*(t) = s_{ij}^0 + T_i \cdot \dot{x}_i(t) + \frac{\dot{x}_i(t) \cdot [\dot{x}_i(t) - \dot{x}_j(t)]}{2\sqrt{A_i d_i}}$ is the desired gap distance between vehicle i and the leading vehicle j (not including the vehicle length), $g_{ij}(t)$ is the current gap distance, s_{ij}^0 is the minimum gap in congested traffic, T_i is the safe time gap of vehicle i for following the leading vehicle j , A_i is the maximum acceleration of vehicle i , d_i is the maximum desired deceleration of vehicle i .

Under steady-state conditions, i.e., $\ddot{x}_i(t) = 0$ and $\dot{x}_i(t) = \bar{x}_i(t)$, we obtain the speed-gap relation as

$$v = v_f \left[1 - (g^*/g)^2 \right]^{1/\delta}, \text{ where } g^* = s_0 + v \cdot T \quad (26)$$

and the gap-speed relation as

$$g = (s_0 + v \cdot T) \cdot \left[1 - (\nu/v_f)^\delta \right]^{-1/2} \quad (27)$$

Then, the spacing-speed relation can be written as

$$s = g + l_p = (s_0 + v \cdot T) \cdot \left[1 - (\nu/v_f)^\delta \right]^{-1/2} + l_p \text{ in } n-t \text{ coordinate} \quad (28)$$

where l_p is the average physical vehicle length, s_0 indicates the average value of minimum gap distance, and T denotes the average safe time gap. It should be noted that $s_0 + l_p$ is equal to l in Eq. (7).

Interestingly, based on Eq. (28), two special cases can be written as:

(1) When $\delta = 1$ and $s_0 = 0$, we have

$$V_e(s)|_{\delta=1, s_0=0} = \frac{(s - l_p)^2}{2v_f T^2} \left(-1 + \sqrt{1 + \left(\frac{2T v_f}{s - l_p} \right)^2} \right) \quad (29)$$

(2) When $\delta = 2$ and $s_0 = 0$, we get

$$V_e(s)|_{\delta=2, s_0=0} = v_f \sqrt{\sqrt{1 + \left(\frac{T v_f}{s - l_p} \right)^2}} \quad (30)$$

When $\delta \rightarrow \infty$, according to Eq. (26), $v = v_f$; based on Eq. (28), $s = s_0 + v \cdot T + l_p$, i.e., $s = v \cdot T + l$. Then, the limiting case, i.e., triangular fundamental diagram, is generated as $Q_e(k) = \min[v_f k, (1 - k/k_j)/T]$, that is, one branch represents free-flow states, and another branch indicates congested states. Obviously, macro-IDM and FTSM under the homogeneous case have the same limiting fundamental diagrams only if the average safe time gap T is equal to average response time τ . Based on Eq. (28) in $n-t$ coordinate, two other equivalents can be respectively formulated as

$$k = \left\{ (s_0 + v \cdot T) \cdot \left[1 - (\nu/v_f)^\delta \right]^{-1/2} + l_p \right\}^{-1} \text{ in } x-t \text{ coordinate} \quad (31)$$

or

$$q = kv = v \left\{ (s_0 + v \cdot T) \cdot \left[1 - (\nu/v_f)^\delta \right]^{-1/2} + l_p \right\}^{-1} \text{ in } x-t \text{ coordinate} \quad (32)$$

and

$$p = h \left\{ (s_0 + T/h) \cdot \left[1 - (h_f/h)^\delta \right]^{-1/2} + l_p \right\} \text{ in } x-n \text{ coordinate} \quad (33)$$

In the following, their boundary conditions, i.e., kinematic wave speed, wave flux and wave spacing at jam condition, can be derived as:

In $x-t$ coordinate, based on Eq. (12) and the following expression

$$s' = \left[1 - (\nu/v_f)^\delta \right]^{-1/2} \left\{ T + \frac{\delta}{2v_f} (s_0 + v \cdot T) \left[1 - (\nu/v_f)^\delta \right]^{-1} (\nu/v_f)^{\delta-1} \right\} \quad (34)$$

we obtain

$$\frac{dq}{dk} = v - \frac{\left\{ (s_0 + v \cdot T) \cdot \left[1 - (\nu/v_f)^\delta \right]^{-1/2} + l_p \right\} \left[1 - (\nu/v_f)^\delta \right]}{T \left[1 - (\nu/v_f)^\delta \right]^{1/2} + \frac{\delta}{2v_f} (s_0 + v \cdot T) \left[1 - (\nu/v_f)^\delta \right]^{-1/2} (\nu/v_f)^{\delta-1}} \quad (35)$$

Therefore,

$$\omega_j = \frac{dq}{dk} \Big|_{k=k_j, v=0} = -\frac{s_0 + l_p}{T} = -\frac{l}{T} \quad (36)$$

In $n-t$ coordinate, based on Eq. (34), we have

$$\frac{dv}{ds} \Big|_{s=l, v=0} = \left\{ \left[1 - (\nu/v_f)^\delta \right]^{-1/2} \left\{ T + \frac{\delta}{2v_f} (s_0 + v \cdot T) \left[1 - (\nu/v_f)^\delta \right]^{-1} (\nu/v_f)^{\delta-1} \right\} \right\}^{-1} \Big|_{s=l, v=0} = \frac{1}{T} \quad (37)$$

In $x-n$ coordinate, based on Eqs. (17, 18, 34), we obtain

$$\left. \frac{dh}{dp} \right|_{p=\infty, s=l, v=0} = \frac{1}{s - v ds/dv} \Big|_{p=\infty, s=l, v=0} = \frac{1}{l}, \text{ i.e., } \left. \frac{dp}{dh} \right|_{h=\infty, s=l, v=0} = l. \quad (38)$$

3.3.3. Related analyses for LCM

Enough attention should be paid to LCM (Ni et al., 2015), which successfully bridge the microscopic driving behaviors to fundamental diagrams. Its microscopic model (i.e., micro-LCM) is formulated as

$$\ddot{x}_i(t + \tau_i) = A_i \left[1 - \frac{\dot{x}_i(t)}{v_i} - e^{1 - s_{ij}(t)/s_{ij}^*(t)} \right] \quad (39)$$

Moreover, its macroscopic counterpart (i.e., macro-LCM) with three representations are expressed respectively as

$$k = (rv^2 + \tau v + l)^{-1} [1 - \ln(1 - v/v_f)]^{-1} \text{ in } x-t \text{ coordinate} \quad (40)$$

or

$$q = kv = v(rv^2 + \tau v + l)^{-1} [1 - \ln(1 - v/v_f)]^{-1} \text{ in } x-t \text{ coordinate} \quad (41)$$

$$s = (rv^2 + \tau v + l) [1 - \ln(1 - v/v_f)] \text{ in } n-t \text{ coordinate} \quad (42)$$

$$p = h(rh^{-2} + \tau h^{-1} + l) [1 - \ln(1 - h_f/h)] \text{ in } x-n \text{ coordinate} \quad (43)$$

Accordingly, their boundary conditions are respectively derived as

$$\left. \frac{dq}{dk} \right|_{k=k_j, v=0} = -\frac{l}{\tau + l/v_f} \quad (44)$$

$$\left. \frac{dv}{ds} \right|_{s=l, v=0} = \frac{1}{\tau + l/v_f} \quad (45)$$

$$\left. \frac{dp}{dh} \right|_{h=\infty, s=l, v=0} = l \quad (46)$$

Based on above mentioned formulations of three macro-models and their property analyses, it is concluded that when $T = \tau$, FTSM under the homogeneous case and macro-IDM have the same limiting case of bilinear fundamental relations, and their kinematic wave speed (wave flux or wave spacing) values at jam condition are also the same. However, macro-LCM has the different kinematic wave speed and wave flux values when traffic is jammed. For better comparison, Table 1 lists their formulations with three representations and corresponding kinematic wave speed, wave flux and wave spacing at jam condition.

4. Empirical studies

4.1. Calibration methodology

To fit the fundamental diagrams with three representations to real-world traffic data, a bi-level optimization procedure is employed here, which is similar to Rakha and Arafah (2010). First, each set of raw data is aggregated to reduce its size to a manageable level. When aggregating the data set, e.g., density and flux data, the entire range of one independent variable (i.e., density) is delimited into numbers of equal intervals, and then the density data and flux data (i.e., dependent variable) falling within these intervals are aggregated by computing an empirical mean (abbreviated as *Emp mean*). Based on these two kinds of aggregated traffic data, other traffic variables in Eulerian and Lagrangian coordinates are also derived with their relationships defined in Eq. (4). Next, the bi-level optimization procedure is carried out based on these aggregated data. The inner loop searches for the minimum distance from each dot of “*Emp mean*” (e.g., q_e , v_e and k_e) to the fundamental diagram curve (\bar{q}_e , \bar{v}_e and \bar{k}_e) normalized by (q_{\max} , v_{\max} and k_{\max}) given a set of model parameters, which can be written as

$$\min d_e = \sqrt{\left(\frac{q_e - \bar{q}_e}{q_{\max}} \right)^2 + \left(\frac{v_e - \bar{v}_e}{v_{\max}} \right)^2 + \left(\frac{k_e - \bar{k}_e}{k_{\max}} \right)^2} \quad (47)$$

Here, q_{\max} , v_{\max} and k_{\max} respectively denote the maximum values of “*Emp mean*” flux, speed and density.

Then, the outer loop searches for a set of optimized parameters that minimize the total of minimized distance, that is,

$$\min D = \sum d_e \text{ subject to the model parameters.} \quad (48)$$

Table 1

Comparison of three traffic stream models in three coordinates.

Coordinates	FTSM	Macro-IDM	Macro-LCM
(x-t)	$q = v(rv^2 + \tau v + l)^{-1} [1 - (v/v_f)^\delta]^{1/\sigma}$ $\frac{dq}{dk} _{k=k_j, v=0} = -\frac{1}{\tau}$	$q = v\{(s_0 + v \cdot T) \cdot [1 - (v/v_f)^\delta]^{-1/2} + l_p\}^{-1}$ $\frac{dq}{dk} _{k=k_j, v=0} = -\frac{s_0 + l_p}{T} = -\frac{1}{\tau}$	$q = v(rv^2 + \tau v + l)^{-1} [1 - \ln(1 - v/v_f)]^{-1}$ $\frac{dq}{dk} _{k=k_j, v=0} = -\frac{1}{\tau + l/v_f}$
(n-t)	$s = (rv^2 + \tau v + l)[1 - (v/v_f)^\delta]^{-1/\sigma}$ $\frac{ds}{dv} _{s=l, v=0} = \frac{1}{\tau}$	$s = (s_0 + v \cdot T) \cdot [1 - (v/v_f)^\delta]^{-1/2} + l_p$ $\frac{ds}{dv} _{s=l, v=0} = \frac{1}{T}$	$s = (rv^2 + \tau v + l)[1 - \ln(1 - v/v_f)]$ $\frac{ds}{dv} _{s=l, v=0} = \frac{1}{\tau + l/v_f}$
(x-n)	$p = h(rh^{-2} + \tau h^{-1} + l)[1 - (h_f/h)^\delta]^{-1/\sigma}$ $\frac{dp}{dh} _{h=\infty, s=l, v=0} = l$	$p = h\{(s_0 + T/h) \cdot [1 - (h_f/h)^\delta]^{-1/2} + l_p\}$ $\frac{dp}{dh} _{h=\infty, s=l, v=0} = l$	$p = h(rh^{-2} + \tau h^{-1} + l)[1 - \ln(1 - h_f/h)]$ $\frac{dp}{dh} _{h=\infty, s=l, v=0} = l$

Here, in the outer loop, one heuristic algorithm named monkey algorithm (MA) with dynamic adaptation (DAMA) proposed by Zheng (2013), with strong global optimization capability for the multi-extremal optimization problem, is employed to search for the optimal model parameters. For more introductions about MA and DAMA, please refer to Appendix B. Moreover, the number of equal intervals in the outer loop to reflect the aggregation level, and the step size in the inner loop designed to search the closest point of one “*Emp mean*” in the fundamental diagram curve, play an important role in the total calculated distance, which will be examined by the following sensitivity analyses.

4.2. Calibration and result analyses

Usually, traffic flow exhibits facility- or location-specific fundamental relations. To verify the flexibility of FTSM, loop/microwave detector data from a wide range of facilities are utilized to carry out the calibration tasks. First, field traffic data selected from five locations are described as follows.

- (I) Loop detector 868, 856, 845 and 831 are the facilities selected in Minisoda, and their flux and occupancy data for every 5 min are extracted during 2016/03/23–2016/03/29. (II) The flux and occupancy data for every 5 min in I-5 of Seattle are drawn from loop detector 14 and 18, and these datasets last for a period of 2011/08/01–2011/08/31. (III) In I-205 of Portland, loop detector 1378 and 1387 are the selected facilities, whose flux and speed data for every 5 min are picked out during 2011/09/15–2011/11/15. (IV) Loop detector data of station 1108148 and 1108291 in I-5 of San Diego come from PeMS, which cover flux and speed data for every 5 min during 2010/11/16–2010/11/19. The two stations are both located in mainline and respectively have 6 and 5 lanes. (V) In 3rd ring of Beijing, microwave detector data of station 3040 and 3044 are collected during 2012/03/01–2012/03/31, which cover the flux and speed data for every 2 min.

As for loop detector data from Minisoda and Seattle, the occupancy data are transformed into density data by $k = o/L$, where o is the time occupancy, and L the total length of the averaged vehicle and loop detector. Here, L is approximately equal to 6 m. Then, the entire density range of each dataset is divided into 300 equal intervals, and the empirical mean flux, density and speed are calculated for each interval, which are referred as the aggregated data. After that, above mentioned calibration methodology with parameters of DAMA listed in Table 2 is employed to make FTSM fit these aggregated traffic data (Note: the step size in the inner loop is set as 0.01 m/s), and the calibration results refer to Table 3. Besides, taking the evolution of measured distance (MD) calculated by Eq. (48) and six parameters based on field data from #14 in Seattle as an example (c.f., Fig. 2), the performance index judged by MD nearly converges to its minima in the 2nd cycle, and six parameters gradually evolve to their own optimal values. This implies the well optimization capability of this calibration methodology.

Table 3 shows that various fitting results are generated at various places due to the location-specific potential fundamental relations, and #14 #1387 #1108291 and #3040 have the relatively better calibration results respectively in Minisoda, Seattle, Portland, San Diego and Beijing. Thus, Figs. 3–7 illustrate their fitted FTSMs three representations, which include the flux-density, speed-density and speed-flux relations in Eulerian coordinate system, and the speed-spacing and time headway-pace relations in two Lagrangian coordinate systems. Especially, Figs. 3(a) and 4(a) demonstrate that the fitted flux-density curves exhibit the (slight) mirrored-lambda shape, and such shape is more apparent in Fig. 4(a). Moreover, the fitted flux-density curves in Fig. 5(a) and Fig. 6(a) both take a nearly triangular shape, while that in Fig. 7(a) shows a parabolic shape. This implies the very well flexibility of FTSM. Additionally, all of these fitted curves almost run through the dots of aggregated data or the intermediate zone between fluctuant dots, exhibiting the satisfactory fitting performance. From Figs. 3(b)–(e), 4(b)–(e), 5(b)–(e), 6(b)–(e), 7(b)–(e), it is seen that other fundamental relations also follow the trend nicely of corresponding aggregated data, further verifying the flexibility of FTSM with other representations and effectiveness of the calibration methodology.

Besides, these fitted fundamental curves can generally capture the key information about the aggregated data, such as the capacity points and their corresponding turning points in other coordinates. This helps provide some practical and meaningful suggestions for LOS analysis and transportation planning. Interestingly, it should be noted that the (slight) mirrored-lambda shape appears in Figs. 3(a) and 4(a), which can be seen as a combination of concave, straight and convex sections. This seems conflicting with a desirable property of flux-density relationship, i.e., concavity. However, such shape comes from

Table 2
Parameters for DAMA.

Parameters	DAMA
Population size	5
Step length	0.1 * UP
Climb number	50
Eyesight	0.01aUP
Watch times	10
Cyclic number	50
$\sigma/\delta\kappa$	10/10/10
$C(0)$	0.08

Table 3
Calibration results based on real-field traffic data from various facilities.

Location	Loop/Station ID	Estimated parameters	MD
Minisoda	#868	$\tau = 1.69 \text{ s}, r = -0.0106 \text{ s}^2/\text{m}, l = 6.49 \text{ m}, v_f = 16.9 \text{ m/s}, \delta = 26.8, \sigma = 1.63$	1.0037
	#856	$\tau = 1.26 \text{ s}, r = -0.0112 \text{ s}^2/\text{m}, l = 11.3 \text{ m}, v_f = 24.0 \text{ m/s}, \delta = 32.0, \sigma = 0.50$	0.6603
	#845	$\tau = 1.48 \text{ s}, r = -0.0126 \text{ s}^2/\text{m}, l = 11.1 \text{ m}, v_f = 28.6 \text{ m/s}, \delta = 50.0, \sigma = 1.12$	0.4974
	#831	$\tau = 1.18 \text{ s}, r = -0.0138 \text{ s}^2/\text{m}, l = 12.9 \text{ m}, v_f = 20.8 \text{ m/s}, \delta = 30.1, \sigma = 1.59$	0.6730
Seattle	#14	$\tau = 1.97 \text{ s}, r = -0.0138 \text{ s}^2/\text{m}, l = 5.32 \text{ m}, v_f = 35.5 \text{ m/s}, \delta = 31.7, \sigma = 1.65$	0.2776
	#18	$\tau = 1.96 \text{ s}, r = -0.0037 \text{ s}^2/\text{m}, l = 5.58 \text{ m}, v_f = 29.8 \text{ m/s}, \delta = 19.1, \sigma = 2.75$	0.3839
Portland	#1378	$\tau = 1.79 \text{ s}, r = -0.0113 \text{ s}^2/\text{m}, l = 13.1 \text{ m}, v_f = 28.5 \text{ m/s}, \delta = 30.0, \sigma = 0.80$	1.4033
	#1387	$\tau = 1.42 \text{ s}, r = -0.0119 \text{ s}^2/\text{m}, l = 12.9 \text{ m}, v_f = 27.1 \text{ m/s}, \delta = 20.7, \sigma = 0.50$	0.5056
San Diego	#1108148	$\tau = 1.72 \text{ s}, r = -0.0104 \text{ s}^2/\text{m}, l = 15.0 \text{ m}, v_f = 31.1 \text{ m/s}, \delta = 40.3, \sigma = 0.50$	0.2548
	#1108291	$\tau = 1.96 \text{ s}, r = -0.0043 \text{ s}^2/\text{m}, l = 15.0 \text{ m}, v_f = 31.5 \text{ m/s}, \delta = 17.9, \sigma = 0.77$	0.1864
	#3040	$\tau = 1.33 \text{ s}, r = -0.0059 \text{ s}^2/\text{m}, l = 5.00 \text{ m}, v_f = 18.2 \text{ m/s}, \delta = 1.16, \sigma = 4.27$	0.9244
Beijing	#3044	$\tau = 0.94 \text{ s}, r = -0.0081 \text{ s}^2/\text{m}, l = 5.00 \text{ m}, v_f = 20.2 \text{ m/s}, \delta = 1.01, \sigma = 2.07$	1.6296

the real field data and has also been reported by [Koshi et al. \(1983\)](#), [Banks \(1989\)](#) and [Ni et al. \(2015\)](#). FTSM is just verified to have the excellent flexibility under certain combinations of parameters, and its reproduction of the mirrored-lambda shape should not be treated as its weakness.

Furthermore, the novel representation of FTSM, i.e., time headway-pace relation, is convex and different from flux-density and speed-spacing relations, which are usually concave (c.f., [Figs. 3–7](#)). Their further differences exist in the fact that flux-density-speed relations and speed-spacing relation are only related to traffic state or estimation of traffic state, while time headway-pace relation gives out directly the travel time information per vehicle unit or distance unit and their mapping relation. Combing the time headway-pace equilibrium relation and travel time conservation equation generates the travel time kinematic wave model (i.e., T-model in [Laval and Leclercq \(2013\)](#)), which can be discretized by Godunov scheme to describe the travel time dynamics per vehicle unit and per distance unit. Then, by incorporating the travel time-related field data observed and data-assimilation technique ([Haykin, 2001](#)), the travel time information can be directly estimated. For similar studies, please refer to [Yuan \(2013\)](#). Therefore, this allows us to understand the traffic phenomena from a completely new viewpoint.

4.3. Comparison of fitting performance

In order to verify the superiority of FTSM in fitting the empirical traffic data, this section introduces another seven fundamental relations besides of macro-IDM and macro-LCM. Their expressions are respectively formulated as:

(a) Greenshields model ([Greenshields, 1935](#)):

$$V_e(k) = v_f(1 - k/k_f);$$

(b) Greenberg model ([Greenberg, 1959](#)):

$$V_e(k) = v_c \ln(k_f/k);$$

(c) Underwood model ([Underwood, 1961](#)):

$$V_e(k) = v_f e^{-k/k_c};$$

(d) Northwestern model ([Drake et al., 1967](#)):

$$V_e(k) = v_f e^{-0.5(k/k_c)^2};$$

(e) [Del Castillo and Benítez \(1995\)](#)'s fundamental relation:

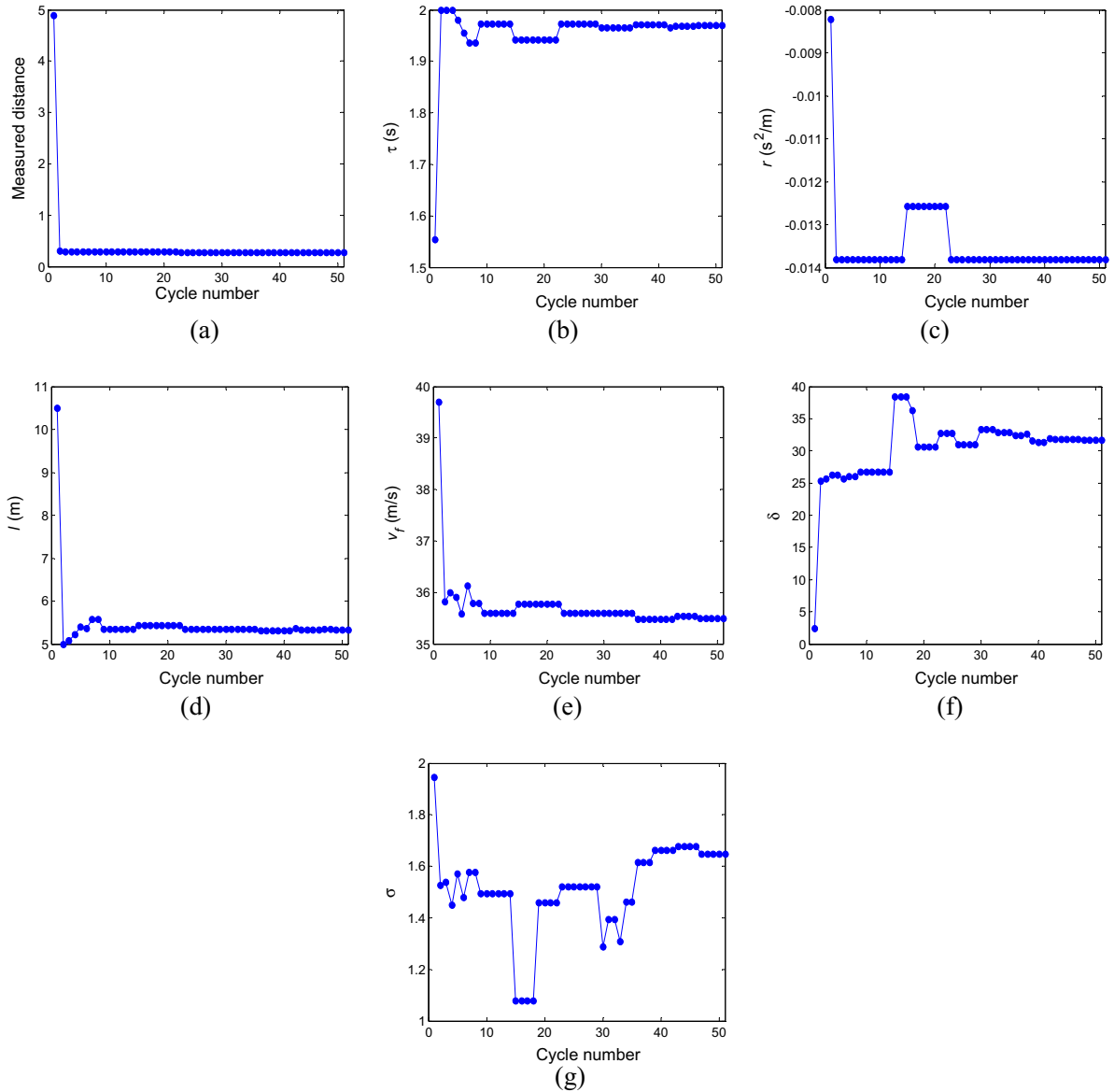


Fig. 2. Evolution processes based on field data from #14 in Seattle.

$$V_e(k) = v_f \left[1 - \exp \left(1 - \exp \left(\frac{\omega_j}{v_f} \left(\frac{k_j}{k} - 1 \right) \right) \right) \right];$$

(f) Negative power function (Del Castillo, 2012):

$$q_n(k) = \omega_j k_j [(v_f k / \omega_j k_j)^{-\omega} + (1 - k / k_j)^{-\omega}]^{-1/\omega};$$

(g) Smulders (1990)' fundamental relation:

$$V_e(k) = \begin{cases} v_f - \frac{v_f - v_c}{k_c} k, & \text{if } k < k_c; \\ \frac{k_c v_c}{k_j - k_c} \left(\frac{k_j}{k} - 1 \right), & \text{if } k \geq k_c. \end{cases}$$

where ω is the shape parameter, and v_c is the critical velocity at the critical density k_c .

First of all, field data from loop detector #1378 in Portland are employed again to calibrate other nine fundamental relations and the calibration results are listed in Table 4. Obviously, FTSM obtains the best fitting performance due to the small-

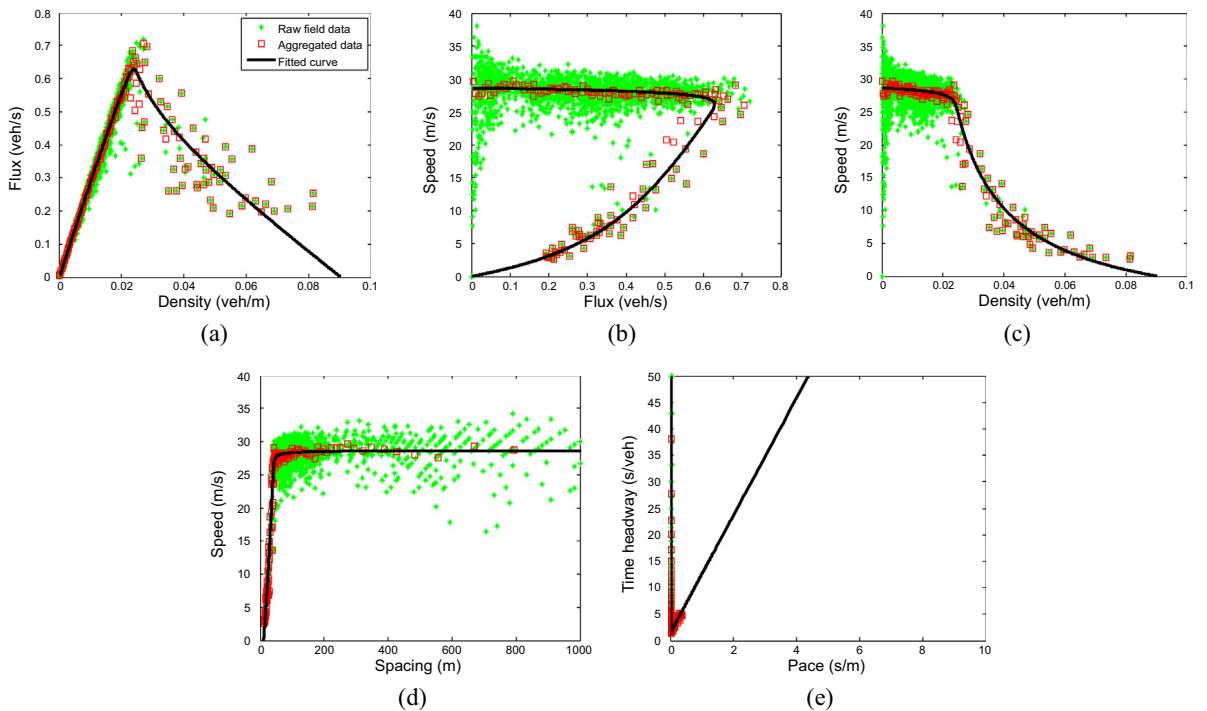


Fig. 3. Fitting performance of FTSM with three representations based on field data from #845 in Minisoda.

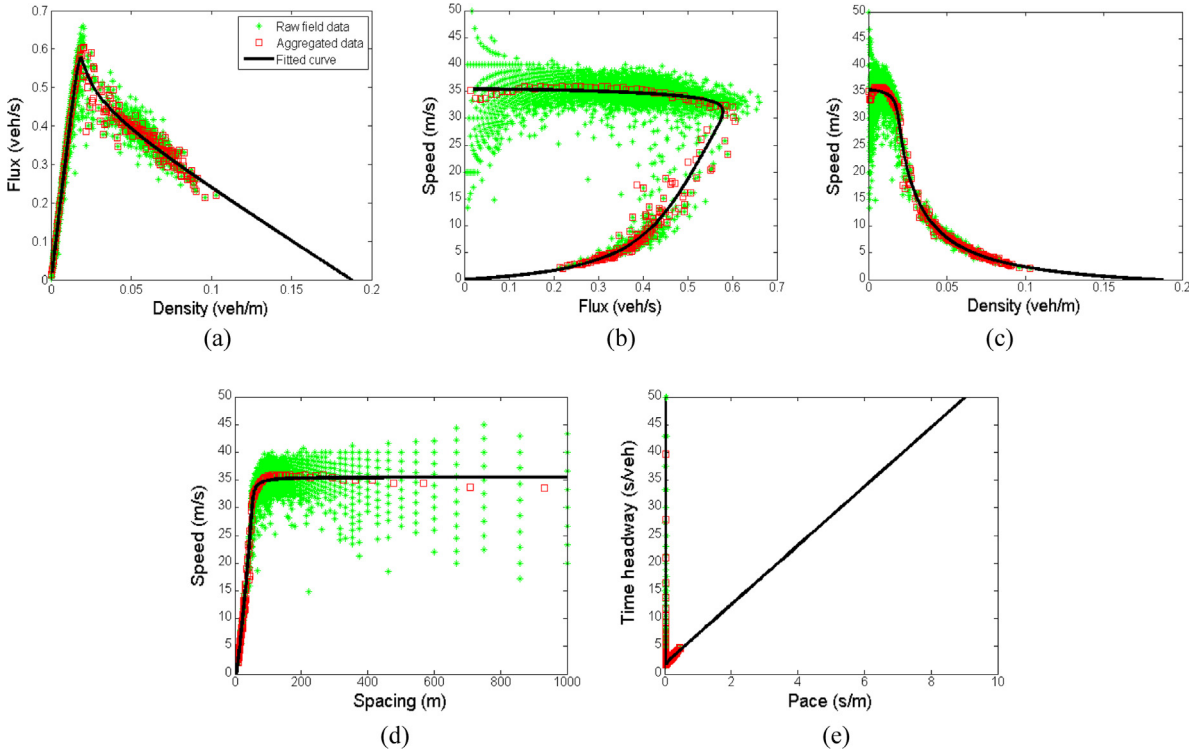


Fig. 4. Fitting performance of FTSM with three representations based on field data from #14 in Seattle.

est MD. However, Smulders, macro-IDM, Negative power function and macro-LCM have the similar performance to FTSM, and their calibrated jam densities are all in the range of (0.07, 0.08) veh/m and free-flow speeds in the range of (26, 28) m/s . Their similar performance can also be demonstrated by the fitted fundamental curves with three representations in

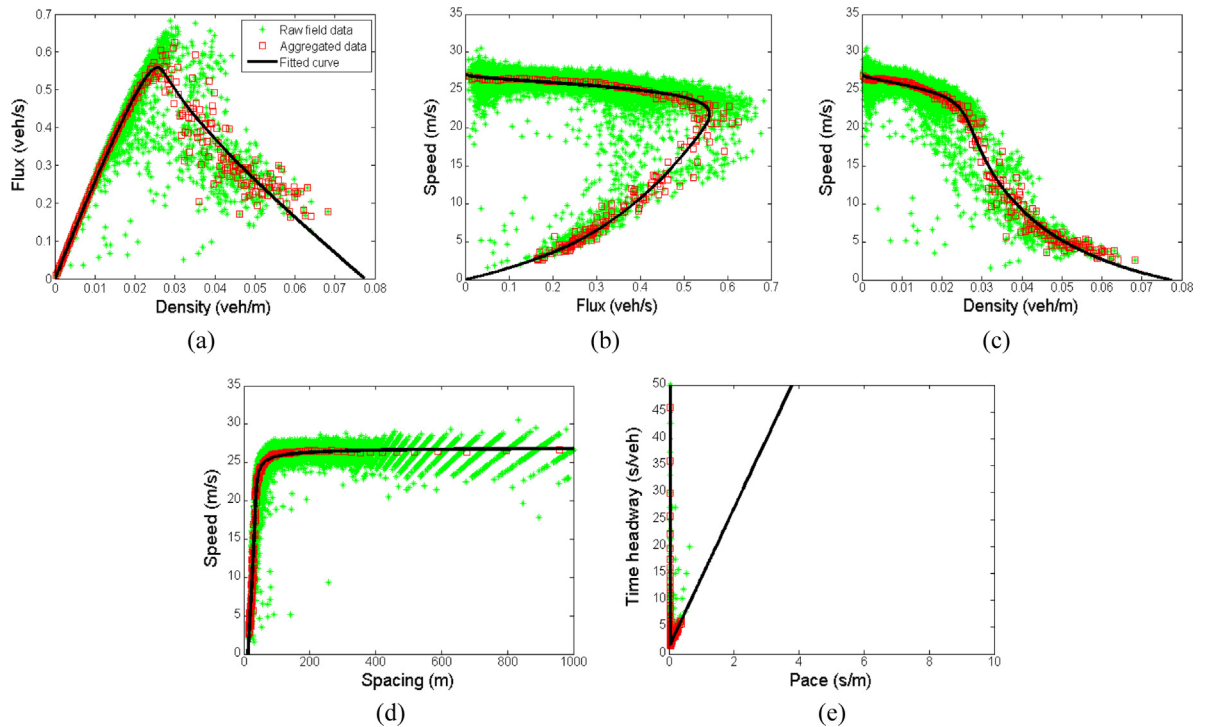


Fig. 5. Fitting performance of FTSM with three representations based on field data from #1387 in Portland.

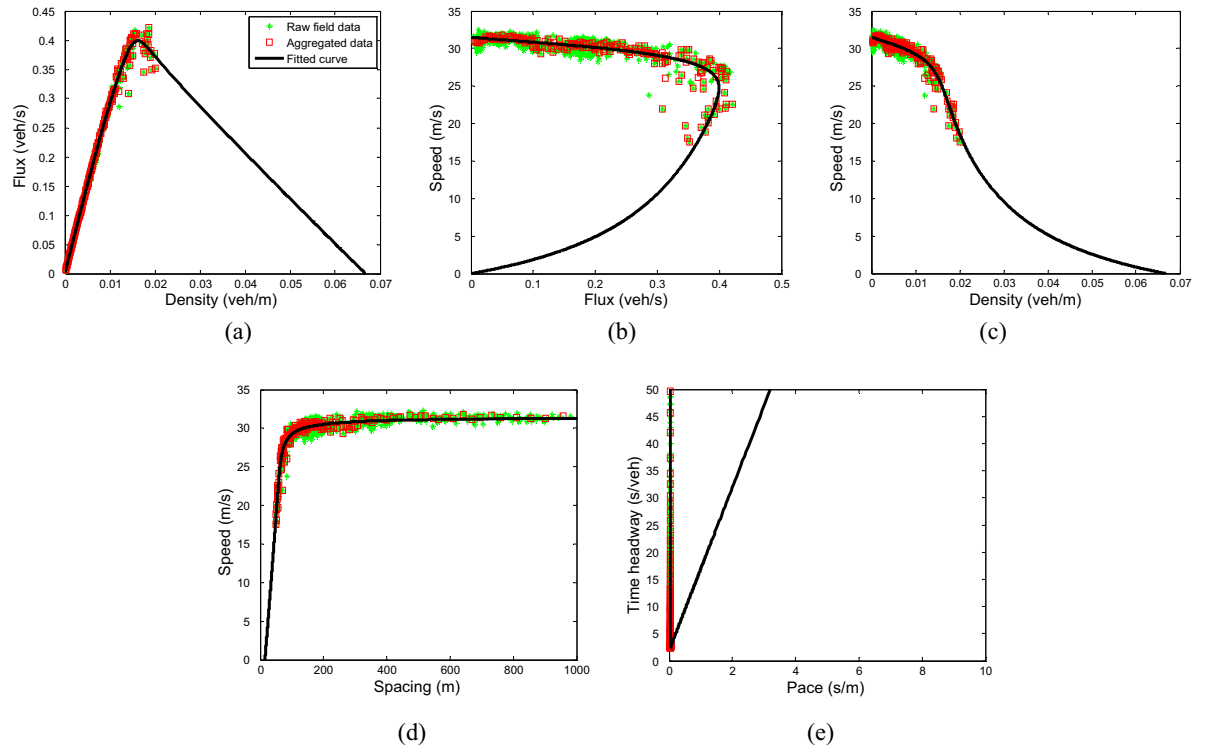


Fig. 6. Fitting performance of FTSM with three representations based on field data from #1108291 in San Diego.

Fig. 8. Besides, by comparison of calibration results for these ten fundamental relations, the fitting performance tends to be better as the number of model parameters increases. That is also to say, the fundamental relations with more degrees of freedom generally exhibit the better flexibility to fit real-world traffic data.

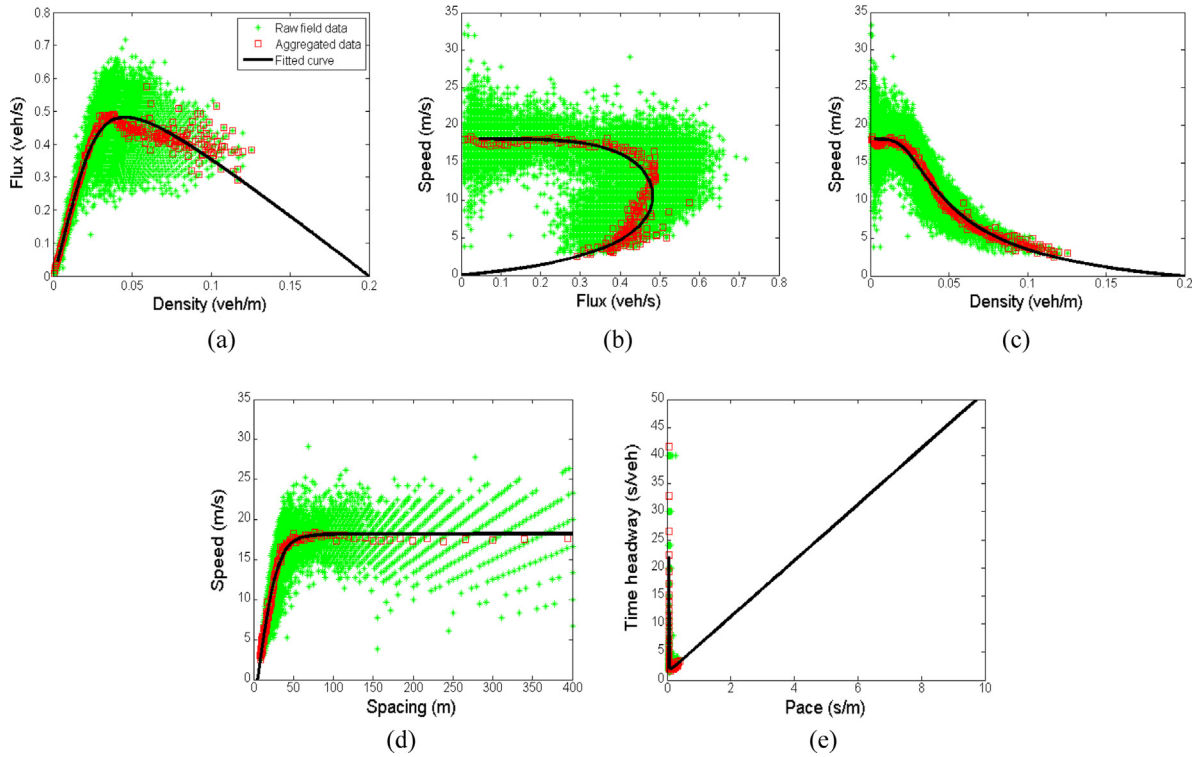


Fig. 7. Fitting performance of FTSM with three representations based on field data from #3040 in Beijing.

Table 4

Comparison of calibration results based on field data from loop detector #1378 in Portland.

Model	Estimated parameters	MD
Greenshields	$k_j = 0.052 \text{ veh/m}$, $v_f = 34.0 \text{ m/s}$	3.7037
Greenberg	$k_j = 0.069 \text{ veh/m}$, $v_c = 14.4 \text{ m/s}$	7.8605
Underwood	$k_c = 0.025 \text{ veh/m}$, $v_f = 40.0 \text{ m/s}$	6.6734
Northwestern	$k_c = 0.028 \text{ veh/m}$, $v_f = 30.8 \text{ m/s}$	2.4776
Del Castillo and Benitez	$k_j = 0.069 \text{ veh/m}$, $\omega_j = 10.0 \text{ m/s}$, $v_f = 28.0 \text{ m/s}$	2.9685
Negative power function	$k_j = 0.072 \text{ veh/m}$, $\omega_j = 9.00 \text{ m/s}$, $v_f = 27.7 \text{ m/s}$, $\omega = 13.3$	1.5160
Smulders	$k_c = 0.018 \text{ veh/m}$, $k_j = 0.071 \text{ veh/m}$, $v_c = 26.3 \text{ m/s}$, $v_f = 28.8 \text{ m/s}$	1.4865
Macro-IDM	$T = 1.54 \text{ s}$, $s_0 = 9.09 \text{ m}$, $l = 5.00 \text{ m}$, $v_f = 28.1 \text{ m/s}$, $\delta = 27.7$	1.4883
Macro-LCM	$\tau = 0.97 \text{ s}$, $r = -0.0340 \text{ s}^2/\text{m}$, $l = 14.2 \text{ m}$, $v_f = 28.1 \text{ m/s}$	1.7868
FTSM	$\tau = 1.79 \text{ s}$, $r = -0.0113 \text{ s}^2/\text{m}$, $l = 13.1 \text{ m}$, $v_f = 28.5 \text{ m/s}$, $\delta = 30.0$, $\sigma = 0.80$	1.4033

Moreover, further comparison of fitting performance by these fundamental relations is carried out based on the field data from loop detector #14 in Seattle, which aims to validate the significant superiority of FTSM. The calibration results in Table 5 also show that FTSM has the best capability of adjusting its fundamental curves to fit the field data. However, macro-IDM, Smulders, Negative power function and macro-LCM occupy the relatively closer fitting performance to FTSM, and their free-flow speeds are all around 35.5 m/s and jam densities all near 0.15 veh/m, which is apparently smaller than that of FTSM (i.e., about 0.188 veh/m). In Fig. 9, the fitted fundamental curves also demonstrate that FTSM outperforms all others, and exhibits the mirrored-lambda shape, following nicely the trend of aggregated data. Meanwhile, the fitting results generally become better as the number of model parameters increases, which accords with the conclusion aforementioned. From above comparison it is easily known that the best fitting performance is usually generated along with the largest number of model parameters that need to be calibrated, i.e., FTSM. This may take the most cost, but DAMA incorporated in the calibration methodology has the advantage of dealing with the high-dimensional optimization problem, without (much) worsening the optimization efficiency and capability, which has been validated by Zheng (2013).

In addition, sensitivity analyses about the aggregation level in the outer loop (c.f., Fig. 10(a)) show that the smaller number of equal intervals (i.e., the higher aggregation level) results in the smaller measured distance and FTSM usually performs better than other four models. Especially, when the number of equal intervals decreases to 20, measured distances for FTSM, macro-LCM, macro-IDM and Smulder almost coincide with each other. Therefore, the superiority of FTSM appears more significantly when the aggregation level is lower, e.g., 300 equal intervals. On the other hand, sensitivity analyses about

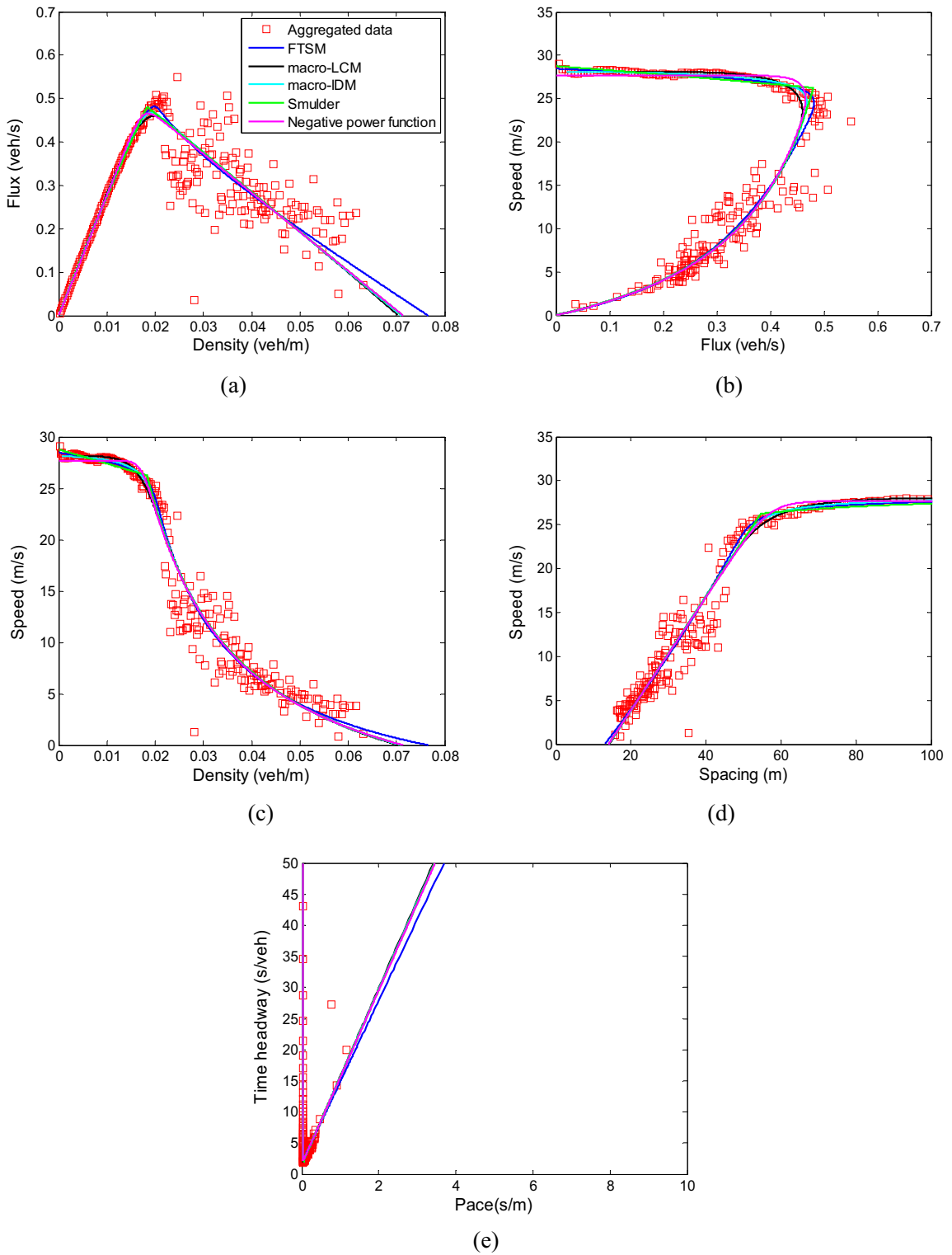


Fig. 8. Fitting performance comparison with field data from loop detector #1378 in Portland.

the step size in the inner loop (c.f., Fig. 10(b)) show that the larger step size (i.e., the lower resolution level) generally results in the higher measured distance, that is, the larger step size introduces the larger inaccuracy when searching the nearest points on the fitted curve. However, FTSM generally outperforms other four models. Note that the step size in Fig. 10(b1)

Table 5

Comparison of calibration results based on field data from loop detector #14 in Seattle.

Model	Estimated parameters	MD
Greenshields	$k_j = 0.071 \text{ veh/m}$, $v_f = 37.8 \text{ m/s}$	4.7026
Greenberg	$k_j = 0.095 \text{ veh/m}$, $v_c = 14.6 \text{ m/s}$	4.4724
Underwood	$k_c = 0.033 \text{ veh/m}$, $v_f = 40.0 \text{ m/s}$	3.7345
Northwestern	$k_c = 0.031 \text{ veh/m}$, $v_f = 35.4 \text{ m/s}$	3.5438
Del Castillo and Benitez	$k_j = 0.145 \text{ veh/m}$, $\omega_j = 4.38 \text{ m/s}$, $v_f = 40.0 \text{ m/s}$	1.5603
Negative power function	$k_j = 0.154 \text{ veh/m}$, $\omega_j = 3.91 \text{ m/s}$, $v_f = 35.1 \text{ m/s}$, $\omega = 49.8$	0.3715
Smulders	$k_c = 0.016 \text{ veh/m}$, $k_j = 0.154 \text{ veh/m}$, $v_c = 34.6 \text{ m/s}$, $v_f = 35.5 \text{ m/s}$	0.3713
Macro-IDM	$T = 1.65 \text{ s}$, $s_0 = 0.84 \text{ m}$, $l = 5.71 \text{ m}$, $v_f = 35.4 \text{ m/s}$, $\delta = 50$	0.3695
Macro-LCM	$\tau = 1.41 \text{ s}$, $r = -0.0322 \text{ s}^2/\text{m}$, $l = 6.62 \text{ m}$, $v_f = 35.8 \text{ m/s}$	0.5970
FTSM	$\tau = 1.97 \text{ s}$, $r = -0.0138 \text{ s}^2/\text{m}$, $l = 5.32 \text{ m}$, $v_f = 35.5 \text{ m/s}$, $\delta = 31.7$, $\sigma = 1.65$	0.2776

is designed based on the speed value due to Eq. (8) or Eq. (9), which is difficult to be solved to explicit flux-density relation. While the step size in Fig. 10(b2) is set according to the density value because the negative power function is hard to be transformed into explicit flux-speed relation as Eq. (9) presents. Definitely, the resolution level judged by the step size in Fig. 10(b2) is much higher than that in Fig. 10(b1) so as to sufficiently verify the outperformance of FTSM.

5. Applications

The proposed novel car-following model (c.f., Eq. (1)) and FTSM can be easily applied to investigate traffic phenomena at both microscopic and macroscopic levels, because both of them take the simple mathematical formulations involving physically meaningful parameters. For illustrative purposes, a concrete example similar to that in Ni et al. (2015) is designed, in which a sluggish truck from an on-ramp creates a moving bottleneck in a highway and finally exits from an off-ramp. Through microscopic modeling, profiles of vehicle trajectories generated by this car-following model can be expressed as three representations, respectively on x - t , n - t and x - n coordinates. In this condition, the cause and effect of vehicles' slowing down or speeding up can be analyzed in exhaustive detail from three different perspectives. On the other hand, the macroscopic modeling allows FTSM to produce corresponding fundamental diagrams with three representations, which helps determine the shock paths and shock waves in three coordinates.

Before presenting this illustrative example, based on Rankine-Hugoniot jump condition (Rankine, 1870; Hugoniot, 1887; Evans, 1998), the slopes of shock wave in x - t , n - t , and x - n coordinates are respectively defined as

$$\begin{cases} U_{xt} = [q]/[k] \\ U_{nt} = [\nu]/[s] \\ U_{xn} = [p]/[h] \end{cases} \quad (49)$$

where $[\cdot]$ is an operator that takes the difference of traffic states at both sides of a shock wave boundary.

Then, the numerical example is described as follows. A freeway segment contains an on-ramp (which is located at 1000 m away from a reference point denoting the upstream boundary of the freeway) followed by an off-ramp 2400 m apart. Initially, the freeway operates under a free flow state, i.e., one vehicle enters the freeway segment every 10 s with the free-flow speed 24 m/s. At 65 s, a slow truck enters the freeway from the on-ramp traveling at a speed of 8 m/s, which forces the traffic to operate under the congested state. After 300 s, the truck leaves the freeway at the downstream off-ramp. Then, the traffic would recover from the congested state and operate under the capacity condition. The impact of the slow truck on the traffic will be illustrated microscopically and macroscopically by numerical experiments.

Moreover, the impact on vehicle trajectories and shock waves in three coordinates due to three critical model parameters (i.e., the spacing-related sensitivity σ , speed-related sensitivity δ and calmness parameter r) will be analyzed in detail at both micro- and macro-levels.

5.1. Case one

Fundamental diagrams with three representations, illustrated in Fig. 11, are generated using FTSM to characterize the freeway with the following parameters: free-flow speed $v_f = 24 \text{ m/s}$, calmness parameter $r = -0.028 \text{ s}^2/\text{m}$, average response time $\tau = 1.0 \text{ s}$, effective vehicle length $l = 7.5 \text{ m}$, speed-related sensitivity $\delta = 0.5$, and spacing-related sensitivity $\sigma = 2$ and 4. According to these two parametrized FTSMs, three traffic states under $\sigma = 2$ are derived, i.e., the free-flow state A ($k = 0.0042 \text{ veh/m}$, $q = 0.1 \text{ veh/s}$, $v = 23.8095 \text{ m/s}$), the congested state B ($k = 0.0474 \text{ veh/m}$, $q = 0.3794 \text{ veh/s}$, $v = 8 \text{ m/s}$), and the capacity condition C ($k = 0.0303 \text{ veh/m}$, $q = 0.4250 \text{ veh/s}$, $v = 14.0264 \text{ m/s}$); those under $\sigma = 4$ are obtained, i.e., the free-flow state A' ($k = 0.0042 \text{ veh/m}$, $q = 0.1 \text{ veh/s}$, $v = 23.8095 \text{ m/s}$), the congested state B' ($k = 0.0588 \text{ veh/m}$, $q = 0.4706 \text{ veh/s}$, $v = 8 \text{ m/s}$), and the capacity condition C' ($k = 0.0345 \text{ veh/m}$, $q = 0.6683 \text{ veh/s}$, $v = 19.3710 \text{ m/s}$).

Based on the connection between various traffic variables (shown as the black dotted lines in Fig. 11), these traffic states (A/B/C and A'/B'/C') can be converted to their equivalents in speed-spacing curves and time headway-pace curves. Then, the

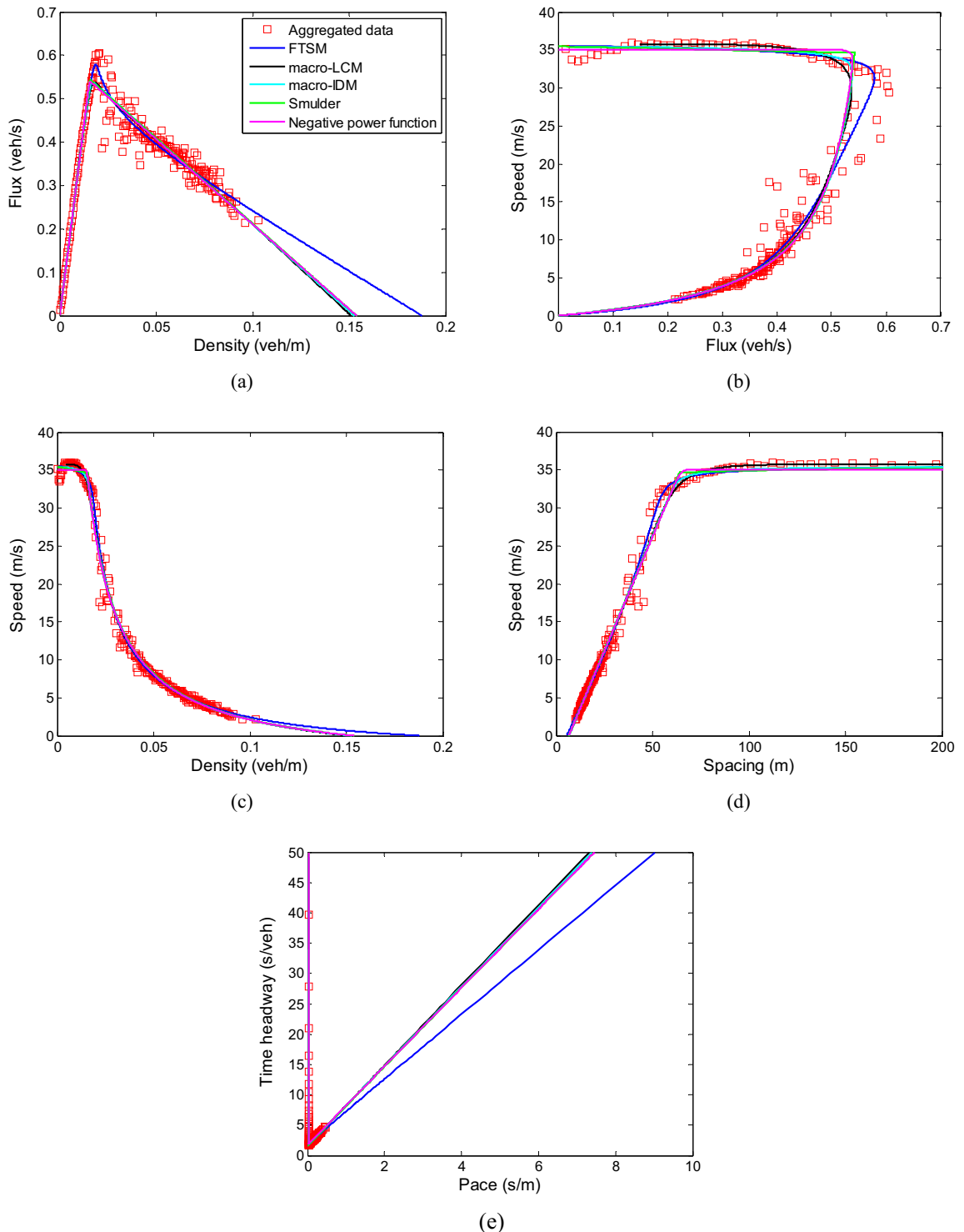


Fig. 9. Fitting performance comparison with field data from loop detector #14 in Seattle.

graphical solutions to find shock paths (which delineate regions of different traffic conditions) on x - t coordinate can also be transformed to those on Lagrangian coordinates, i.e., $(n-t)$ and $(x-n)$. In Fig. 11, the red¹ solid lines and red dotted lines indicate the equivalent shock paths for $\sigma = 2$ and 4 respectively. Their slope values for shock waves connecting two traffic states are

¹ For interpretation of color in Figs. 11–13 and 15, the reader is referred to the web version of this article.

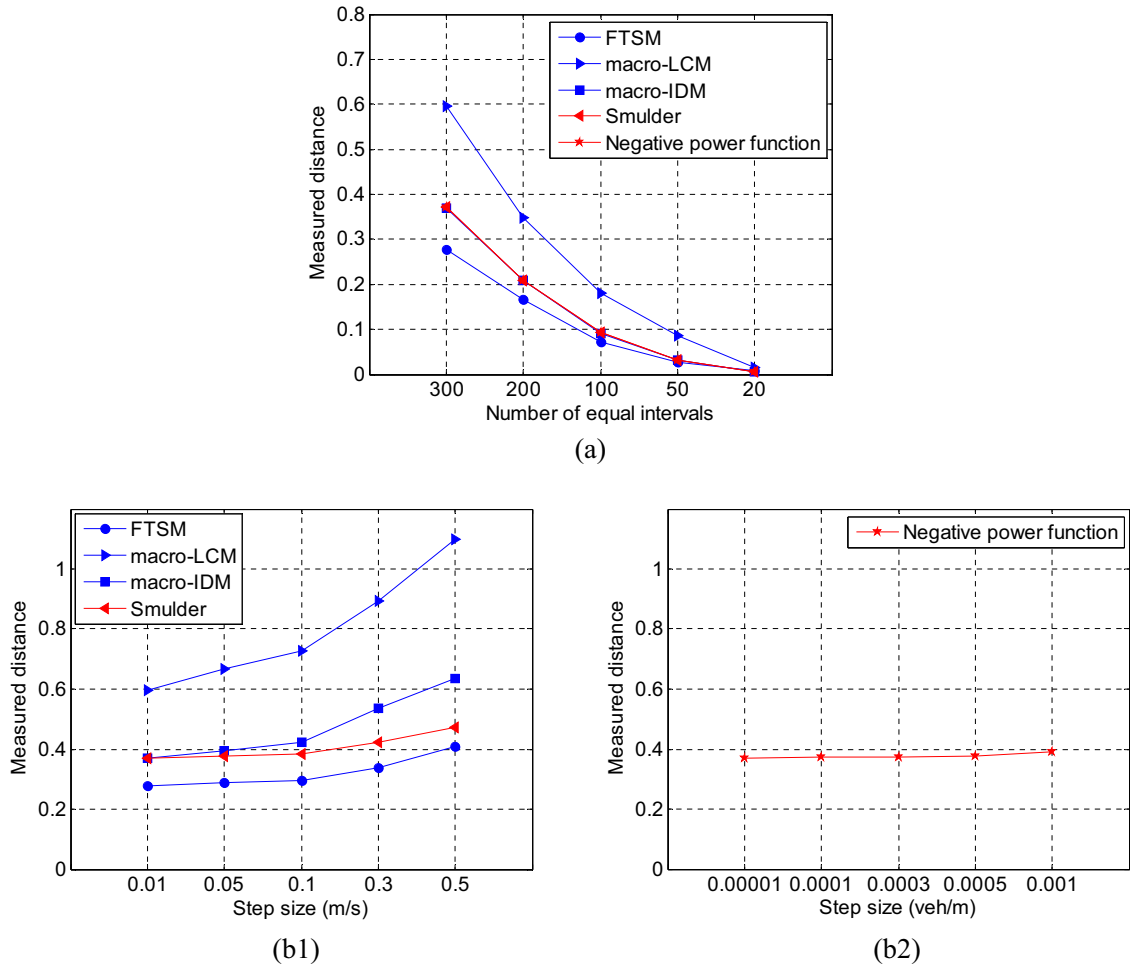


Fig. 10. Sensitivity analyses based on field data from loop detector #14 in Seattle.

determined according to Eq. (49) and the results are listed in Table 6. Obviously, various slopes result from varying fundamental diagrams in three coordinates, whose shapes are dependent on the spacing-related sensitivity σ . To verify whether the macroscopic and microscopic solutions agree with each other reasonably, especially at the aspects of shock path and the slope of shock wave, the car-following model formulated as Eq. (1) is employed to conduct the micro-simulation with the following parameters: $v_i = 24 \text{ m/s}$, $A_i = 4 \text{ m/s}^2$, $B_j = 6 \text{ m/s}^2$, $b_i = 9 \text{ m/s}^2$, $\tau_i = 1.0 \text{ s}$, $l_j = 7.5 \text{ m}$, $\delta = 0.5$, and $\sigma = 2$ and 4, where $i \in \{1, 2, 3, \dots, n\}$ are unique identifiers. One vehicle arrives at the upstream boundary of the freeway every 10 s, which corresponds to a flow of $q = 0.1 \text{ veh/s}$, that is, the free-flow region is produced and the traffic is at condition A (A'). The simulation time step is 0.5 s and the simulation duration is 900 s.

For better intuitive understanding, the traffic phenomena and their physical meanings are first explained by vehicle trajectories on x - t plane, c.f., Fig. 12(a) and (d). The first vehicle is set as the slow truck from the on-ramp and its trajectory is predetermined, whereas the motions of other vehicles are determined by Eq. (1). Obviously, this numerical example involves three traffic processes as the following.

5.2. Process one

Before the first vehicle enters the freeway, the second vehicle and vehicles thereafter run nearly at a free-flow speed. At time $t = 65 \text{ s}$, the slow truck enters the freeway, and meanwhile the second vehicle is about to reach the on-ramp. Then, the truck makes its following vehicles adopt nearly the same slow speed, resulting in a congested region B (B'). As the upstream fast platoon A (A') catch up with and join the downstream slow platoon B (B'), the interface of congested region B and free-flow region A (region B' and region A'), P_1P_2 ($P'_1P'_2$), indicates the corresponding shock path; **Process two:** The queue keeps growing until the truck exits from the off-ramp at $t = 365 \text{ s}$. After that, vehicles at the head of the queue begin to accelerate according to Eq. (1), and the congestion starts to discharge at capacity condition C (C'). Therefore, the front of the queue

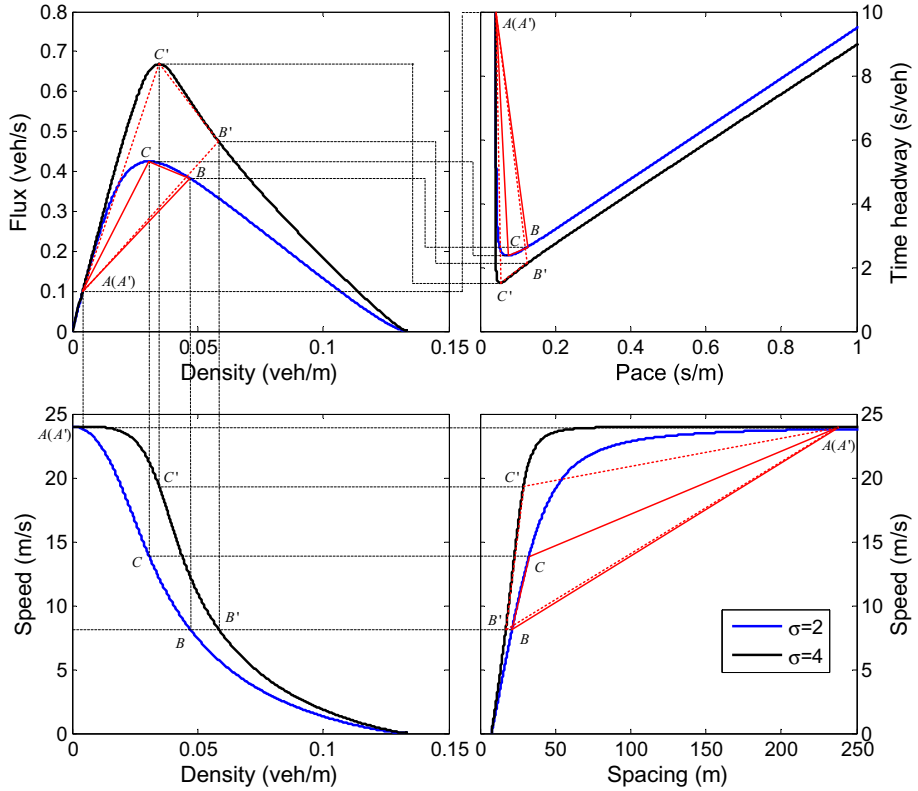


Fig. 11. Fundamental diagrams and equivalent shock paths with three representations under two σ values.

Table 6

Slopes of shock waves with three representations under two σ values.

	Connection	$Q_e(k)$ (m/s)	$V_e(s)$ (veh/s)	$P_e(h)$ (m/veh)
$\sigma = 2$	A-B	6.4676	0.0729	-88.7261
	B-C	-2.6667	0.5062	5.2657
	A-C	12.4521	0.0477	-261.0444
$\sigma = 4$	A'-B'	6.7875	0.0715	-94.8802
	B'-C'	-8.1358	0.9493	8.5670
	A'-C'	18.7558	0.0212	-883.6337

shrinks, leaving a shock path P_3P_2 ($P'_3P'_2$) that separates region C (C') from region B (B'). Finally, the queue front meets the queue tail at P_2 (P'_2), because the former shrinks faster than the latter grows, denoting the ending of both shock paths and the end of congestion. **Process three:** After the congestion disappears, a capacity flow C (C') is followed by a lighter and faster flow A (A'), which comes from the remaining impact of the slow truck. Hence, the trace where the faster platoon A (A') joins the platoon C (C') indicates a shock path P_2P_4 ($P'_2P'_4$).

Moreover, the vehicle trajectories in x - t coordinate can be expressed as “vehicle trajectories” with other two representations, i.e., on n - t plane and x - n plane respectively. A few regions with clearly visible boundaries can be easily distinguished by the varying density of trajectories, which exhibit various characteristics in various coordinates (c.f., Fig. 12). Especially, vehicle trajectories and shock waves on n - t and x - n coordinates provide a completely new perspective to revisit the traffic phenomena aforementioned. By comparison of shock waves on three coordinates (c.f., Fig. 12), it is easily known that on x - t coordinate, the shock wave forms when the fast vehicle platoon catches up with the slow platoon ahead, and vice versa, the slope of vehicle trajectory denotes the vehicle speed and the denser vehicle trajectories mean the higher density. On n - t coordinate, the shock wave is produced when the traffic region with the higher flux meets that with the lower flux, and vice versa, the slope of vehicle trajectory indicates the flux value and the denser vehicle trajectories imply the more smooth traffic flow. It should be noted that the slopes of shock waves are always positive according to the increasing relation between speed and spacing (c.f., Fig. 11). On x - n coordinate, the shock wave is generated when the traffic region with the higher density joins that with the lower density, and vice versa. The absolute slope of vehicle trajectory is traffic spacing

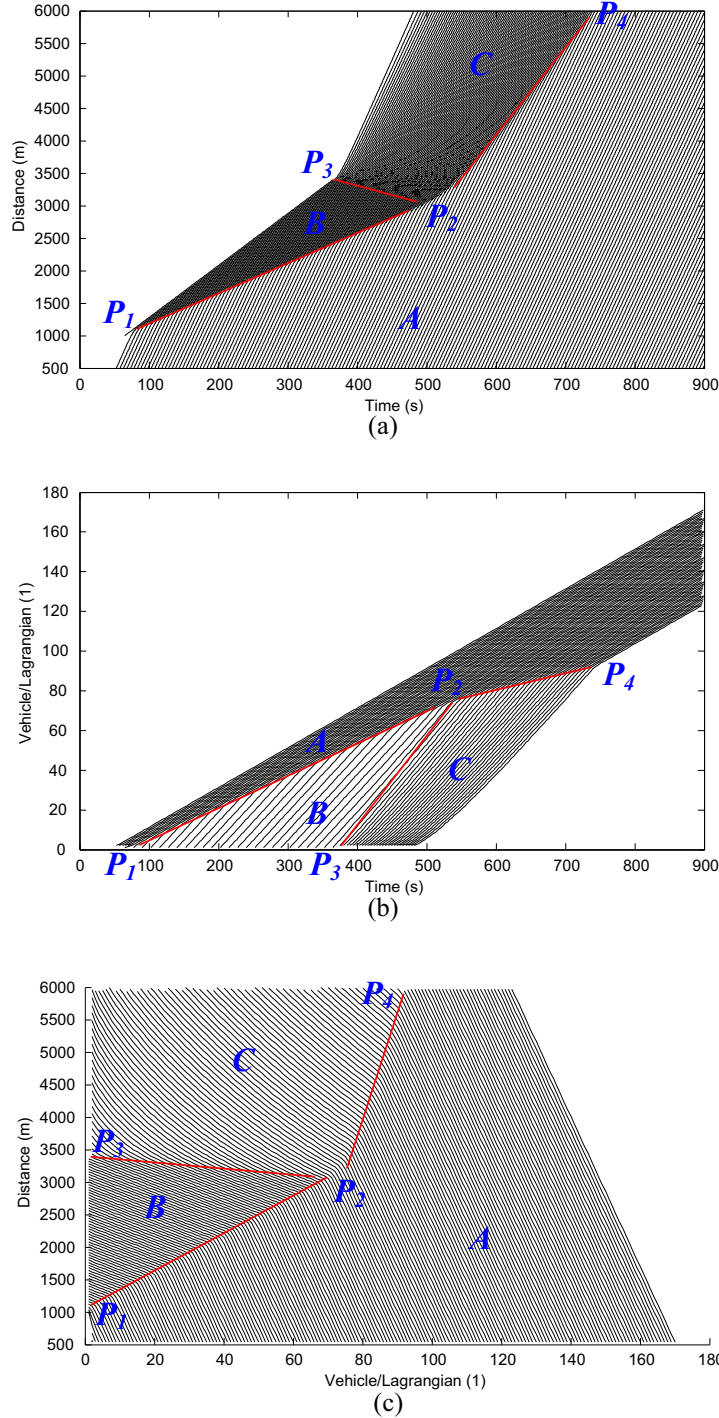
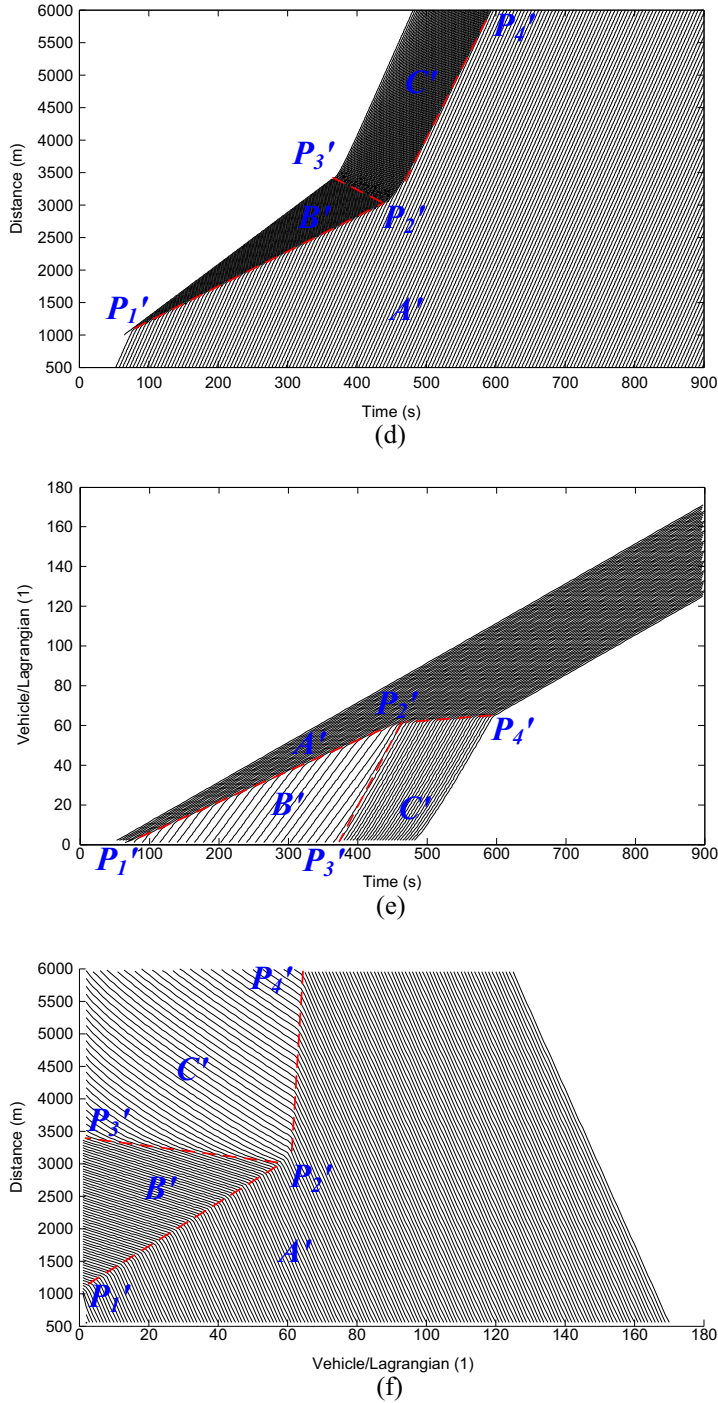


Fig. 12. Vehicle trajectories on three coordinates under two σ values.

information and the larger absolute slope represents the smoother traffic flow. The reason of adding the term “absolute” is due to that the vehicle number increases as the location decreases.

Although the microscopic simulation contains much more information about the motion of each individual vehicle, the temporal-spatial formation and dissipation of congestion, the comparison of the macroscopic graphical solutions and the simulated vehicle trajectories reveals that macro- and micro-solutions on the shock waves agree with each other very well. Especially, the shock paths (denoted by P₁P₂ (P'₁P'₂), P₃P₂ (P'₃P'₂) and P₂P₄ (P'₂P'₄)) in Fig. 12 accord with the macroscopic

**Fig. 12 (continued)**

graphical solutions indicated by the red solid (red dotted) lines in Fig. 11, and their slopes of shock waves calculated along these shock paths are very approximate to those values listed in Table 6. It should be noted that the absolute slopes of these shock paths indicated in time headway-pace curves (c.f., Fig. 11 and Table 6) are very close to those illustrated on x - n plane (c.f., Fig. 12), but they have the opposite signs. This is also due to the fact that the vehicle number increases as the location decreases. Hence, the macro- and micro-solutions on shock waves on x - n coordinate in fact are consistent with each other.

The following is to analyze the impact of σ on the vehicle trajectories and shock waves on three coordinates. As the driver becomes more sensitive to spacing information, i.e., σ gets larger, the vehicle trajectories on three coordinates become more

compact for the congested region and the capacity condition. Three slopes of shock waves (absolute value) on x - t and x - n planes become larger (c.f., Fig. 12(a), (c), (d), (f)). However, slopes of shock waves on n - t plane get smaller for the shock paths connecting the free-flow state and the congested state/capacity condition, while that connecting the congested region and the capacity condition becomes larger (c.f., Fig. 12(b) and (e)). The σ -specific micro-solutions on shock waves can also be proved by the corresponding macro-graphical solutions (c.f., Fig. 11).

5.3. Case two

Similar to **Case one**, this case attempts to study the influence of speed-related parameter δ on vehicle trajectories and shock waves on three coordinates. Thus, four macro-model parameters v_f , r , τ and l , and six micro-model parameters A_i , τ_i , v_i , l_i , b_i and B_j are the same as those in **Case one**. First of all, the fundamental diagrams with three representations, illustrated in Fig. 13, are generated using FTSM with two other parameters: $\delta = 1$ or 2 , and $\sigma = 1$. According to two parametrized FTSMs, three various traffic states under $\delta = 1$ are derived, i.e., the free-flow state A ($k = 0.0045$ veh/m, $q = 0.1$ veh/s, $v = 22.2222$ m/s), the congested state B ($k = 0.0486$ veh/m, $q = 0.3891$ veh/s, $v = 8$ m/s), and the capacity condition C ($k = 0.0402$ veh/m, $q = 0.3969$ veh/s, $v = 9.8731$ m/s); those under $\delta = 2$ are produced, i.e., the free-flow state A' ($k = 0.0043$ veh/m, $q = 0.1$ veh/s, $v = 23.2558$ m/s), the congested state B' ($k = 0.0648$ veh/m, $q = 0.5188$ veh/s, $v = 8$ m/s), and the capacity condition C' ($k = 0.0462$ veh/m, $q = 0.5830$ veh/s, $v = 12.6190$ m/s).

In Fig. 13, the red solid and red dotted lines respectively depict the macroscopic graphical solutions on the shock waves that connect two traffic states under $\delta = 1$ and $\delta = 2$. Their accurate slope values are calculated by Eq. (49) and listed in Table 7. Obviously, the δ -dependent shock waves/shock paths result from δ -specific fundamental diagrams produced on three coordinates. These macroscopic solutions can also be validated with the vehicle trajectories, which are simulated by Eq. (1) with other two parameters, i.e., $\delta = 1$ or 2 , and $\sigma = 1$. Fig. 14 illustrates the simulation results, where the vehicle trajectories are plotted with three representations. The varying density of vehicle trajectories outlines a few regions with clearly visible boundaries, and these regions and boundaries exhibit the distinguishing characteristics on three coordinates. Meanwhile, the comparison of the macro- and micro-solutions on the shock waves uncovers that they accord with each other very well. Especially, the slopes of shock waves calculated along the shock paths (denoted by P_1P_2 ($P'_1P'_2$), P_3P_2 ($P'_3P'_2$) and P_2P_4 ($P'_2P'_4$)) in Fig. 14 are very close to those values in Table 7, and their shock paths (c.f., Figs. 13 and 14) are also consistent with each other.

Moreover, the impact of speed-related parameter δ on the vehicle trajectories and shock waves on three coordinates is analyzed as follows. As the driver becomes more sensitive to the speed information, i.e., δ gets larger, the vehicle trajectories on three coordinates become denser for the congested region and the capacity condition. Therefore, three slopes of shock waves (absolute value) on x - t and x - n planes all become larger (c.f., Fig. 14(a), (c), (d) and (f)). Two shock waves on n - t plane get slower for the paths that connect the free-flow state and the congested state/capacity condition, while the slope of the shock wave connecting the congested region and the capacity condition becomes larger (c.f., Fig. 14(b) and (e)). The δ -dependent micro-solutions on shock waves can also be verified by the corresponding macro-graphical solutions (c.f., Fig. 13).

5.4. Case three

Combined with the second scenario in **Case one** (i.e., $\sigma = 4$), this case tries to study the effect of calmness parameter r on the vehicle trajectories and shock waves on three coordinates. Thus, five macro-model parameters v_f , τ , l , δ and σ , and seven micro-model parameters A_i , τ_i , v_i , l_i , B_j , δ and σ are the same as those values in the second scenario in **Case one**. First, the fundamental diagrams with three representations, demonstrated in Fig. 15, are created using FTSM with another parameter: $r = 0$ s^2/m and -0.028 s^2/m . Based on these two parametrized FTSMs, three traffic states under $r = 0$ s^2/m can be obtained, i.e., the free-flow state A ($k = 0.0042$ veh/m, $q = 0.1$ veh/s, $v = 23.8095$ m/s), the congested state B ($k = 0.0520$ veh/m, $q = 0.4162$ veh/s, $v = 8$ m/s), and the capacity condition C ($k = 0.0343$ veh/m, $q = 0.4546$ veh/s, $v = 13.2536$ m/s); under $r = -0.028$ s^2/m , three traffic states A', B' and C' refer to **Case one**.

Similar to **Case one** and **Case two**, the red solid and red dotted lines represent the macroscopic graphical solutions on the shock waves under $r = 0$ and $r = -0.028$ respectively, c.f., Fig. 15, and their slope values calculated by Eq. (49) are listed in Table 8. Obviously, various calmness values make the fundamental diagrams exhibit various shapes, which result in the different shock waves. Meanwhile, these macroscopic solutions can also be proved by vehicle trajectories with three representations, which are simulated using Eq. (1) with another parameter, i.e., $b_i = 6$ m/s^2 and $b_i = 9$ m/s^2 . Fig. 16 demonstrates the simulation results for $b_i = 6$ m/s^2 , where three kinds of vehicle trajectories are plotted on the x - t plane, n - t plane and x - n plane respectively. A few regions with visible boundaries can be easily distinguished through the varying density of trajectories, which also take various characteristics on three coordinates. The simulation results for $b_i = 9$ m/s^2 (c.f., Fig. 12(d)-(f)) have the similar properties. After that, the comparison of the macro- and micro-solutions on shock waves shows that they agree well with each other. Especially, the slopes of shock waves calculated along the shock paths (that denoted by P_1P_2 ($P'_1P'_2$), P_3P_2 ($P'_3P'_2$) and P_2P_4 ($P'_2P'_4$), c.f., Figs. 16 and 12(d)-(f)) are very approximate to those values listed in Table 8, and macro- and micro-shock paths accord well with each other (c.f., Figs. 15, 16 and 12(d)-(f)).

Finally, the impact on the vehicle trajectories and shock waves due to the calmness parameter r is analyzed and demonstrated on three coordinates. As the driver becomes less calm, i.e., r gets smaller, the vehicle trajectories on three coordinates

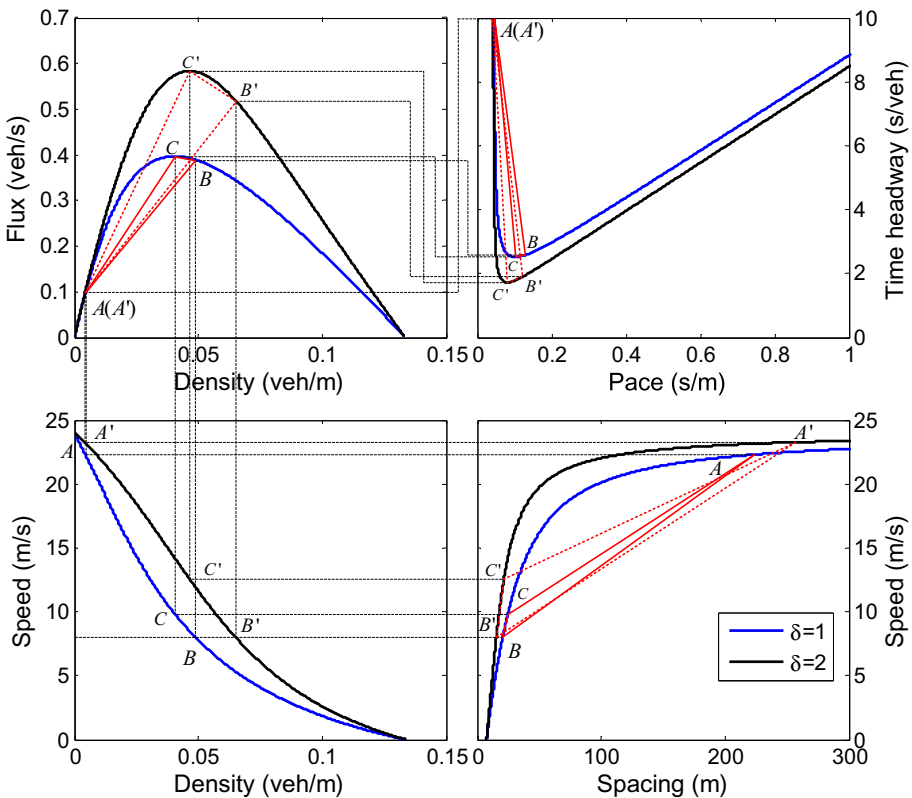


Fig. 13. Fundamental diagrams and equivalent shock paths with three representations under two δ values.

Table 7
Slopes of shock waves with three representations under two δ values.

	Connection	$Q_e(k)$ (m/s)	$V_e(s)$ (veh/s)	$P_e(h)$ (m/veh)
$\delta = 1$	A-B	6.5556	0.0705	-92.8746
	B-C	-0.9286	0.4357	2.1298
	A-C	8.3165	0.0626	-132.9029
$\delta = 2$	A'-B'	6.9223	0.0703	-98.4448
	B'-C'	-3.4516	0.7435	4.6391
	A'-C'	11.5274	0.0504	-228.5724

get closer to each other for the congested region and the capacity condition. Hence, three shock waves with the larger slopes (absolute value) on $x-t$ and $x-n$ planes come into being (c.f., Figs. 16(a) and (c) and 12(d) and (f)). However, on $n-t$ plane two shock waves connecting the free-flow state and the congested state/capacity condition get slower, and that linking the congested region and the capacity condition becomes faster (c.f., Figs. 16(b) and 12(e)). All these changes about micro-solutions on shock waves can be validated by corresponding macro-graphical solutions (c.f., Fig. 15).

6. Conclusions

This work contributes to bridge microscopic driving behaviors with macroscopic traffic phenomena on three coordinates. A traffic stream model named FTSM with the good flexibility is derived from a novel car-following model under steady-state conditions. Its four critical parameters, i.e., calmness parameter, reaction time, speed- and spacing-related sensitivities, can make the fundamental diagrams exhibit various shapes, including the parabolic shape, triangular shape, and even mirrored-lambda shape. By comparison, macro-IDM and FTSM under the homogeneous case have the same limiting fundamental relations (i.e., the triangular shape) and boundary conditions under three representations only if $T = \tau$, while macro-LCM obtains the different boundary conditions under $x-t$ and $n-t$ coordinates. In order to empirically check the flexibility of FTSM, loop/microwave detector data from a wide range of locations, e.g., Minisoda, Seattle, Portland, San Diego, and Beijing, are employed to carry out the calibration tasks with a bi-level optimization procedure. Especially, the optimization algorithm

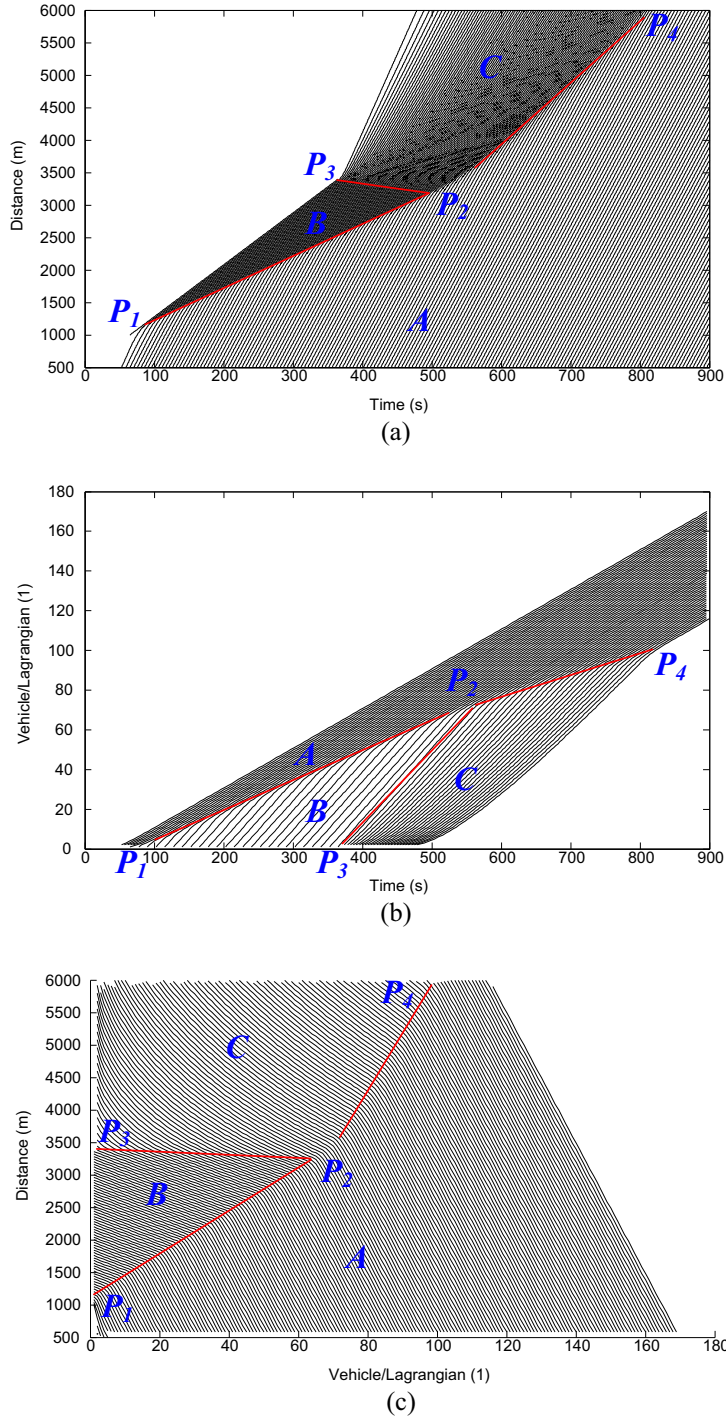


Fig. 14. Vehicle trajectories on three coordinates under two δ values.

in the outer loop applies a recently proposed DAMA, which owns the well global optimization capability. Calibration results show that FTSM fits these field data very well and can take various shapes, including the parabolic, triangular and mirrored-lambda shapes. Meanwhile, FTSM is verified to outperform other nine models by comparing their calibrated results, and the sensitivity analyses about the aggregation level and the step size also prove the superiority of FTSM.

Through the application experiments, macroscopic graphical solutions and microscopic trajectory solutions on shock waves are proved to agree well with each other, and three key parameters, i.e., calmness parameter, speed- and spacing-

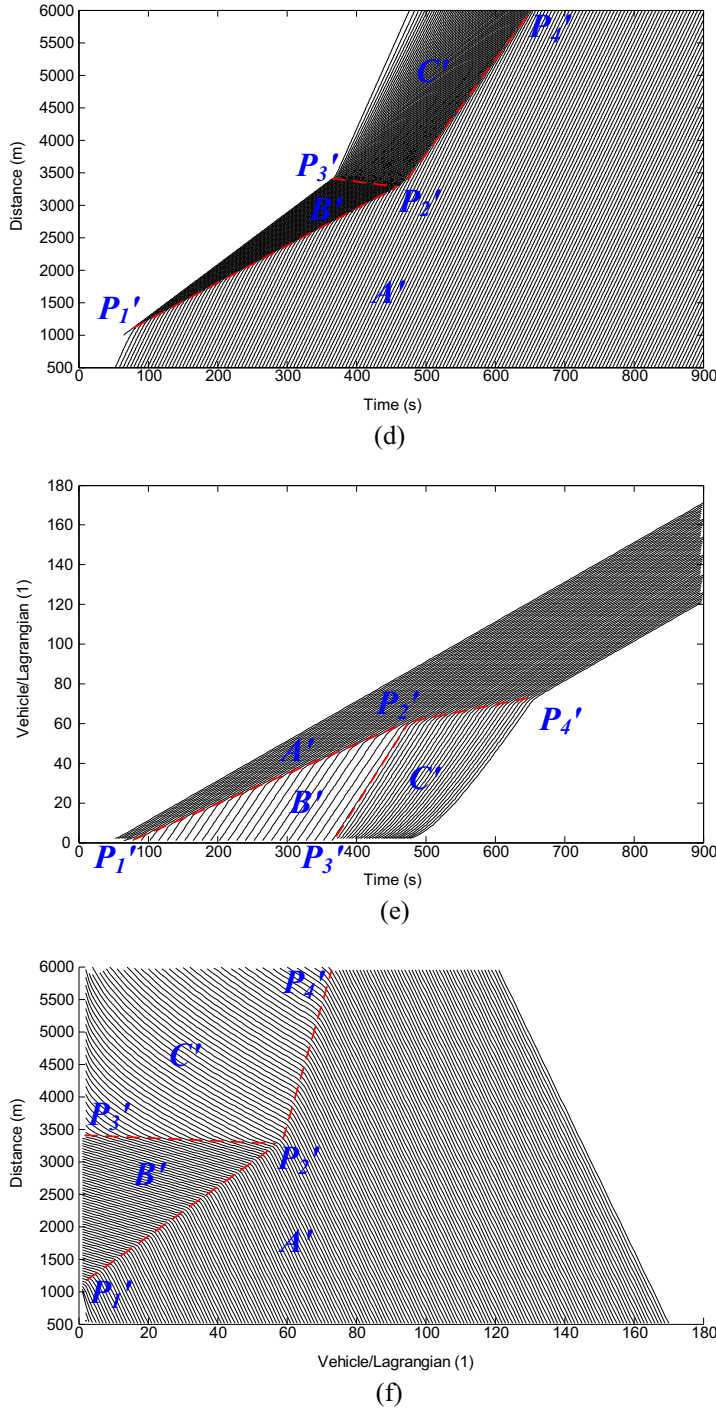


Fig. 14 (continued)

related sensitivities, have the significant influence on vehicle trajectories and shock waves on three coordinates. Especially, vehicle trajectories and shock waves on Lagrangian coordinates, i.e., $(n-t)$ and $(x-n)$, provide a completely new perspective to understand traffic phenomena. It is also found that when drivers become more aggressive, or more sensitive to speed- or spacing-related traffic information, vehicle trajectories with three representations become more compact in the congested region and the capacity condition. All these changes about the shock waves on $x-t$, $n-t$ and $x-n$ planes can be validated by their varying macro-graphical solutions. In summary, FTSM proposed in this paper can not only make the highway capacity and LOS analysis more effective by giving more realistic fundamental diagrams with three representations, but also bridge

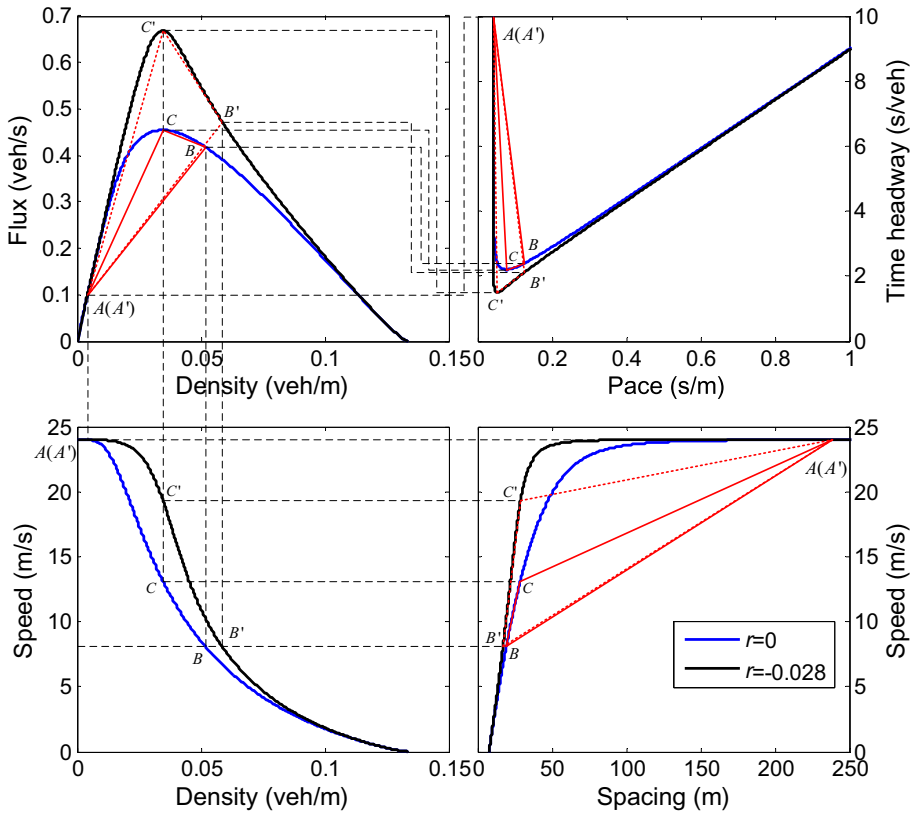


Fig. 15. Fundamental diagrams and equivalent shock paths with three representations under two r values.

Table 8

Slopes of shock waves with three representations under two r values.

	Connection	$Q_e(k)$ (m/s)	$V_e(s)$ (veh/s)	$P_e(h)$ (m/veh)
$r = 0 \text{ s}^2/\text{m}$	A-B	6.6151	0.0722	-91.5339
	B-C	-2.1695	0.5294	4.0961
	A-C	11.7807	0.0505	-233.1837
$r = -0.028 \text{ s}^2/\text{m}$	A'-B'	6.7875	0.0715	-94.8802
	B'-C'	-8.1358	0.9493	8.5670
	A'-C'	18.7558	0.0212	-883.6337

the macroscopic traffic phenomena with microscopic driving behaviors, which benefits to understanding the location-specific driving behaviors.

Acknowledgements

This work is supported by the Natural Science Foundation of China (Nos. 71501191, 71501009) and China Postdoctoral Science Foundation (2014M552165, 2015T80889).

Appendix A

According to the consistency criteria that any car following mode should satisfy (Treiber and Kesting, 2013), the acceleration of Eq. (1) encoding the driving behaviors have been verified to be able to meet the following four requirements.

(1) Based on Eqs. (1) and (2), we have

$$\frac{\partial[\ddot{x}_i(t + \tau_i)]}{\partial[\dot{x}_i(t)]} = -\frac{A_i \delta}{v_i} \left[\frac{\dot{x}_i(t)}{v_i} \right]^{\delta-1} - \frac{A_i \sigma}{s_{ij}(t)} \left[\frac{s_{ij}^*(t)}{s_{ij}(t)} \right]^{\sigma-1} \left[\frac{\dot{x}_i(t)}{b_i} + \tau_i \right]$$

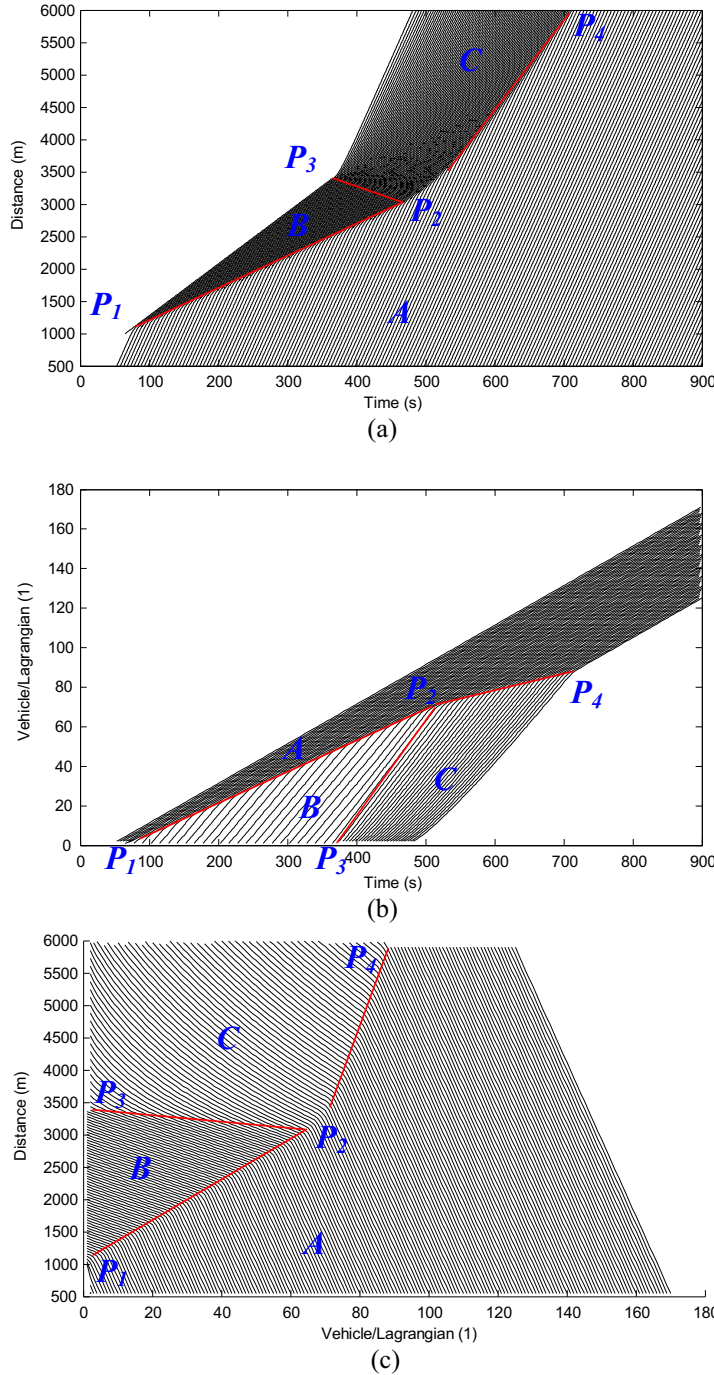


Fig. 16. Vehicle trajectories on three coordinates, $b_i = 6 \text{ m/s}^2$.

Under the constraint $s_{ij}^*(t) \geq l_j$, we obviously obtain $\frac{\partial |\ddot{x}_i(t+\tau_i)|}{\partial |\dot{x}_i(t)|} < 0$. Thus, the acceleration is a strictly decreasing function of the speed.

Meanwhile, as $s_{ij}(t) \rightarrow \infty$, that is, the vehicle i will run freely, the acceleration of vehicle i mainly depends on $\ddot{x}_i(t+\tau_i) = A_i \{1 - [\frac{\dot{x}_i(t)}{v_i}]^\delta\}$. Once $\dot{x}_i(t) \rightarrow v_i$, we get $\ddot{x}_i(t+\tau_i) \rightarrow 0$. Therefore, it is easily gotten that $\lim_{s_{ij}(t) \rightarrow \infty} \ddot{x}_i(t+\tau_i) = 0$. That is also to say, vehicle i accelerates towards a desired speed v_i if not constrained by other vehicles or obstacles.

(2) Similarly, based on Eqs. (1) and (2), we obtain

$$\frac{\partial[\ddot{x}_i(t + \tau_i)]}{\partial[s_{ij}(t)]} = A_i \sigma \left[\frac{\dot{x}_i^2(t)}{2b_i} - \frac{\dot{x}_j^2(t)}{2B_j} + \dot{x}_i \tau_i + l_j \right]^\sigma / [s_{ij}(t)]^{\sigma+1}.$$

Obviously, under the constraint $\frac{\dot{x}_i^2(t)}{2b_i} - \frac{\dot{x}_j^2(t)}{2B_j} + \dot{x}_i \tau_i + l_j \geq l_j$, we have

$$\frac{\partial[\ddot{x}_i(t + \tau_i)]}{\partial[s_{ij}(t)]} \geq 0 \text{ and } \lim_{s_{ij}(t) \rightarrow \infty} \frac{\partial[\ddot{x}_i(t + \tau_i)]}{\partial[s_{ij}(t)]} = 0.$$

Meanwhile, as $s_{ij}(t) \rightarrow \infty$, the vehicle i will run freely and its acceleration value depends on

$$a_{free}[\dot{x}_i(t)] = \lim_{s_{ij}(t) \rightarrow \infty} \ddot{x}_i(t + \tau_i) = A_i \left\{ 1 - \left[\frac{\dot{x}_i(t)}{v_i} \right]^\delta \right\}$$

Obviously, $a_{free}[\dot{x}_i(t)] = \lim_{s_{ij}(t) \rightarrow \infty} \ddot{x}_i(t + \tau_i) \geq \ddot{x}_i(t + \tau_i)$ due to $[s_{ij}^*(t)/s_{ij}(t)]^\sigma > 0$.

Therefore, the acceleration is an increasing function of the spacing $s_{ij}(t)$ to the leading vehicle. Besides, if other vehicles or obstacles are outside the interaction range (i.e., $s_{ij}(t) \rightarrow \infty$), the acceleration does not rely on the spacing value and becomes the free-flow acceleration, which does not get smaller.

(3) Similarly, based on Eqs. (1) and (2), we find

$$\frac{\partial[\ddot{x}_i(t + \tau_i)]}{\partial[\dot{x}_j(t)]} = \frac{A_i \sigma}{B_j} \frac{\dot{x}_j(t)}{s_{ij}(t)} \left[\frac{s_{ij}^*(t)}{s_{ij}(t)} \right]^{\sigma-1} \geq 0, \text{ and } \lim_{s_{ij}(t) \rightarrow \infty} \frac{\partial[\ddot{x}_i(t + \tau_i)]}{\partial[\dot{x}_j(t)]} = 0.$$

Obviously, the acceleration is an increasing function of the speed of the leading vehicle. Together with requirement (1), this also means that the acceleration decreases (the deceleration increases) with the speed of approach to the lead vehicle (or obstacle). Meanwhile, the equality holds if other vehicles (or obstacles) are outside the interaction range (e.g., $s_{ij}(t) \rightarrow \infty$).

(4) Similarly, based on Eqs. (1) and (2), we uncover

When $\dot{x}_i(t) = 0$ and $\dot{x}_j(t) \geq 0$, $s_{ij}^*(t) = \frac{\dot{x}_i^2(t)}{2b_i} - \frac{\dot{x}_j^2(t)}{2B_j} + \dot{x}_i \tau_i + l_j \leq l_j$.

Under the constraint $s_{ij}^*(t) \geq l_j$, it is finally gotten that $s_{ij}^*(t) = l_j$. In this condition, we obtain $\ddot{x}_i(t + \tau_i) = A_i \{ 1 - [l_j/s_{ij}(t)]^\sigma \}$. Obviously, only when $s_{ij}(t)$ is just equal to l_j , it is obtained that $\dot{x}_i(t + \tau_i) = 0$. However, in order to maintain the minimum spacing l_j (even during a standstill) and guarantee no backwards movement if the actual spacing has become smaller than l_j by the past events, we can introduce a buffer distance as the following

$$\ddot{x}_i(t + \tau_i) = \begin{cases} A_i \left\{ 1 - [\dot{x}_i(t)/v_i]^\delta - [s_{ij}^*(t)/s_{ij}(t)]^\sigma \right\}, & s_{ij}(t) > l_j + \varepsilon; \\ A_0, & s_{ij}(t) \leq l_j + \varepsilon. \end{cases}$$

where $\varepsilon > 0$ is designed as the threshold for activating the change of the acceleration (deceleration) mechanism in order to maintain l_j to the leading vehicle, and A_0 is the reasonable acceleration (deceleration) value chosen to make the vehicle being able to maintain l_j to the leading vehicle when the actual spacing is not large than $(l_j + \varepsilon)$. In summary, the first three requirements are completely satisfied, and the fourth requirement is conditionally satisfied. Generally, this car-following model is complete in the sense that it can consistently describe all situations that may arise in single-lane traffic.

Appendix B

Monkey Algorithm originally proposed by Zhao and Tang (2008) is inspired by the mountain-climbing processes of monkeys and mainly consists of climb-process, watch-jump process and somersault process. MA can well deal with the optimization problem of a multimodal function with the decision vector having very large dimensions, which is mainly due to the calculation of the pseudo-gradient of the objective function during climb process. Therefore, MA has been widely applied in various fields, for example, optimal sensor placement (OSP) in structural health monitoring (SHM) (Jia et al., 2015; Yi et al., 2015), power systems optimization (Ituarte-Villarreal et al., 2012). Recently, Zheng (2013) improved original MA from three aspects, that is, (1) the chaotic search was utilized to generate the values of random variables; (2) the step length in climb process decreased dynamically with the evolutionary speed factor; (3) the eyesight, watch times and somersault distance increased dynamically with the aggregation degree. Through performing several test functions, DAMA has been verified to outperform original MA and other heuristic algorithms, e.g., genetic algorithm, particle swarm optimization, etc., in particular when the dimension of the optimization problem is high. The detail steps of DAMA are presented as follows.

B.1. Representation of solution and initialization

- (I) At first the population size of monkeys is set as M , and for any monkey $m \in \{1, 2, \dots, M\}$, its position can be defined as $\chi_m = (\chi_{m1}, \chi_{m2}, \dots, \chi_{md}, \dots, \chi_{mD})$, which express one solution of the optimization problem with D dimensions. Monkeys' feasible positions are generated randomly from an D -dimensional hypercube which contains the potential optimal solutions.
- (II) The idea of chaotic search, instead of random process, is utilized to determine the values of random variable, which can be formulated as

$$O(z+1) = 4 \cdot O(z) \cdot [1 - O(z)]$$

where O is chaotic variable and z is the iteration number. Obviously, the value of O is in the range $(0, 1.0)$, and as long as $O(0) \notin \{0, 0.25, 0.5, 0.75\}$ and the total number of iterations is large enough, O will traverse the whole range $(0, 1.0)$.

B.2. Climb process employed to search the local optima

- (I) The adaptive step length designed for each monkey based on its own evolution state can be expressed as

$$a_m = (1 - h_m/\sigma) \cdot a_m^\psi, \text{ where } h_m = \frac{\min(|f(\chi_m^\psi)|, |f(\chi_m)|)}{\max(|f(\chi_m^\psi)|, |f(\chi_m)|)} \text{ and } 0 \leq h_m \leq 1.$$

The evolutionary speed factor h_m describes the evolution state of monkey m , a_m^ψ and χ_m^ψ are respectively the step length and position of monkey m at the previous cycle, $f(\cdot)$ is the objective function, $1/\sigma$ is the adjustment coefficient of decreasing factor.

- (II) Randomly generate a vector $\Delta\chi_m = (\Delta\chi_{m1}, \Delta\chi_{m2}, \dots, \Delta\chi_{md}, \dots, \Delta\chi_{mD})$, where $\Delta\chi_{md}$ is set as a_m or $-a_m$ with the same possibility, and calculate the pseudo-gradient of the objective function at the position χ_m as

$$f'_m(\chi_m) = \{f'_{m1}(\chi_m), f'_{m2}(\chi_m), \dots, f'_{md}(\chi_m), \dots, f'_{mD}(\chi_m)\} \text{ where } f'_{md}(\chi_m) = [f(\chi_m + \Delta\chi_m) - f(\chi_m - \Delta\chi_m)]/2\Delta\chi_{md}.$$
- (III) Set $y_d = \chi_{md} + a_m \cdot \text{sign}[f'_{md}(\chi_m)]$, $d = 1, 2, \dots, D$ respectively, and let $y = (y_1, y_2, \dots, y_d, \dots, y_D)$.
- (IV) Let $\chi_m \leftarrow y$ provided that y is feasible; Otherwise, χ_m keeps unchanged.
- (V) Repeat step (II) to (IV) until there is little change on the objective function in the neighborhood iterations or the maximum allowable number of iterations N_c has been reached.

B.3. Watch-Jump process to search other better positions

- (I) The adaptive eyesight and watch times dependent on the evolution state of all monkeys are formulated respectively as

$$\beta = (1 + s/\delta) \cdot \beta^\psi \text{ and } w = (1 + s/\kappa) \cdot w^\psi, \text{ where } s = \min(|f_{best}|, |f_{mean}|)/\max(|f_{best}|, |f_{mean}|) \text{ and } 0 \leq s \leq 1.$$

The aggregation degree s describes all monkeys' evolution state, β^ψ and w^ψ are respectively the eyesight and watch times at the previous cycle, f_{best} and f_{mean} are respectively the best fitness among all monkeys and the mean fitness of all monkeys, $1/\delta$ and $1/\kappa$ are the adjustment coefficients of the increasing factor respectively for eyesight and watch times.

- (II) Randomly generate real number y_d from $(\chi_{md} - \beta, \chi_{md} + \beta)$, $d = 1, 2, \dots, D$ respectively. Let $y = (y_1, y_2, \dots, y_d, \dots, y_D)$, β indicates the maximal distance that the monkey can watch.
- (III) Let $\chi_m \leftarrow y$ provided that $f(y) > f(\chi_m)$ and y is feasible. Otherwise, repeat step (II) until an appropriate point y is found or watch times w is reached.
- (IV) Repeat the climb process by employing y as a new initial position.

B.4. Somersault process to make all monkeys transfer to new search domains

- (I) The barycentre of the current positions of all monkeys except monkey m is selected as its somersault pivot and formulated as

$$p = (p_1, p_2, \dots, p_d, \dots, p_D), \text{ where } [p_d = \frac{1}{M-1} \left(\sum_{m=1}^M \chi_{md} - \chi_{md} \right), d = 1, 2, \dots, D].$$

- (II) The position of monkey m is updated along the direction pointing to the pivot as

$$y_d = p_d + \beta \cdot |p_d - \chi_{md}|, d = 1, 2, \dots, D, \text{ where } (p_d - \chi_{md}) \text{ is denoted as the somersault direction of monkey } m.$$
- (III) Set $\chi_m \leftarrow y$ if $y = (y_1, y_2, \dots, y_d, \dots, y_D)$ is feasible. Otherwise, y_d obtains the boundary value.

B.5. Termination

Following the climb process, the watch-jump, and the somersault process, all monkeys are ready for their next cycle. The MA will terminate after a given number (called the cyclic number, denoted by N_m) of cyclic repetitions of the above steps. In summary, the pseudo-code of DAMA can be given as the following Algorithm 1.

Algorithm 1: An Improved Monkey Algorithm with Dynamic Adaptation

INPUT

- 1: Population size of monkeys M , step length a , eyesight β and watch times w
- 2: Initialized position of each monkey χ_m with n dimensions
- BEGIN**
- 3: **For** Cyclic number $ll = 1$ to N_m **do**
- 4: Climb process
- 5: **For** Climb number $kk = 1$ to N_c **do**
- 6: **For** $m = 1$ to M **do**
- 7: Randomly generate a vector $\Delta\chi_m$ and each element is the step length a_m or $-a_m$
- 8: Calculate the pseudo-gradient $f'_m(\chi_m) = \{f'_{m1}(\chi_m), f'_{m2}(\chi_m), \dots, f'_{md}(\chi_m), \dots, f'_{mD}(\chi_m)\}$
- 9: Calculate $y_d = \chi_{md} + a_m \cdot \text{sign}[f'_{md}(\chi_m)]$, $d = 1, 2, \dots, D$
- 10: **If** new position $y = (y_1, y_2, \dots, y_d, \dots, y_D)$ is feasible **then**
- 11: $\chi_m \leftarrow y$
- 12: **Else**
- 13: χ_m is unchanged
- 14: **End if**
- 15: **End for**
- 16: **End for**
- 17: Watch-Jump Process
- 18: **For** $m = 1$ to M **do**
- 19: Randomly generate y_d from $(\chi_{md} - \beta, \chi_{md} + \beta)$, $d = 1, 2, \dots, D$; $n_w = 1$
- 20: **While** $f(y) < f(\chi_m)$ or $y = (y_1, y_2, \dots, y_d, \dots, y_D)$ is not feasible or $n_w < w$ **do**
- 21: Randomly generate y_d from $(\chi_{md} - \beta, \chi_{md} + \beta)$, $d = 1, 2, \dots, D$
- 22: $n_w = n_w + 1$
- 23: **End while**
- 24: $\chi_m \leftarrow y$
- 25: Repeat the climb process with y as the new initial position
- 26: **End for**
- 27: Somersault Process
- 28: **For** $m = 1$ to M **do**
- 29: **For** $d = 1$ to D **do**
- 30: Calculate the somersault pivot $p_d = 1/(M - 1) \cdot (\sum_{m=1}^M \chi_{md} - \chi_{md})$
- 31: Update the position $y_d = p_d + \beta \cdot |p_d - \chi_{md}|$
- 32: **If** y_d is feasible **then**
- 33: $\chi_{md} \leftarrow y_d$
- 34: **Else**
- 35: χ_{md} gets the upper or lower boundary
- 36: **End if**
- 37: **End for**
- 38: **End for**
- 39: Calculate the evolutionary speed factor h_m , $m = 1, 2, \dots, M$
- 40: Update the step length a_m , $m = 1, 2, \dots, M$
- 41: Calculate the aggregation degree of all monkeys s
- 42: Update the eyesight β and watch times w
- 43: **End for**
- OUTPUT**
- 44: Optimal fitness value and optimal solution

References

- Banks, J.H., 1989. Freeway speed-flow-concentration relationships: more evidence and interpretations. *Transp. Res. Rec.* 1225, 53–60.
 Berg, P., Mason, A., Woods, A., 2000. Continuum approach to car-following models. *Phys. Rev. E* 61 (2), 1056–1066.
 Chandler, R.E., Herman, R., Montroll, E.W., 1958. Traffic dynamics: studies in car following. *Oper. Res.* 6 (2), 165–184.

- Claudel, C.G., Bayen, A.M., 2010. Lax-Hopf based incorporation of internal boundary conditions into Hamilton-Jacobi equation. Part I: Theory. Part II: Computational methods. *IEEE Trans. Autom. Control* 55 (5), 1142–1157, 1158–1174.
- Del Castillo, J.M., 2012. Three new models for the flow-density relationship: derivation and testing for freeway and urban data. *Transportmetrica* 8 (6), 443–465.
- Del Castillo, J.M., Benítez, F.G., 1995. On the functional form of the speed-density relationship-I: General theory. *Transp. Res. Part B* 29 (5), 373–389.
- Drake, J.S., Schofer, J.L., May, D.A., 1967. A statistical analysis of speed-density hypotheses. *Highway Res. Rec.* 156, 53–87.
- Edie, L., 1963. Discussion of traffic stream measurements and definitions. In: Almond, J. (Ed.), *Proceedings of the 2nd International Symposium on Transportation and Traffic Theory*. Organization for Economic Cooperation and Development, Paris, France, pp. 139–154.
- Evans, L., 1998. *Partial Differential Equations*. American Mathematical Society.
- Gazis, D., Herman, R., Potts, R., 1959. Car-following theory of steady-state traffic flow. *Oper. Res.* 7 (4), 499–505.
- Greenberg, H., 1959. An analysis of traffic flow. *Oper. Res.* 7, 79–85.
- Greenshields, B.D., 1935. A study in highway capacity. In: *Highway Research Board Proceedings*, vol. 14, pp. 448–477.
- Gupta, A.K., Katiyar, V.K., 2006. A new anisotropic continuum model for traffic flow. *Physica A* 368, 551–559.
- Haykin, S., 2001. *Kalman Filtering and Neural Networks*. John Wiley & Sons, New York, NY.
- Helbing, D., 2009. Derivation of non-local macroscopic traffic equations and consistent traffic pressures from microscopic car-following models. *Eur. Phys. J. B* 69, 539–548.
- Helly, W., 1959. Simulation of bottlenecks in single lane traffic flow. In: *Proceedings of the Symposium on the Theory of Traffic Flow*. Elsevier, New York, NY, pp. 207–238.
- Herrera, J.C., Bayen, A.M., 2010. Incorporation of Lagrangian measurements in freeway traffic state estimation. *Transp. Res. Part B* 44 (4), 460–481.
- Hugoniot, H., 1887. Sur la propagation du mouvement dans les corps et spécialement dans les gaz parfaits (première partie). *Journal de l'École polytechnique* 57, 3–97.
- Ituarte-Villarreal, C., Lopez, N., Espiritu, J., 2012. Using the monkey algorithm for hybrid power systems optimization. *Proc. Comput. Sci.* 12, 344–349.
- Jabari, S., Zheng, J., Liu, H., 2014. A probabilistic stationary speed-density relation based on Newell's simplified car-following model. *Transp. Res. Part B* 68, 205–223.
- Jia, J.Q., Feng, S., Liu, W., 2015. A triaxial accelerometer monkey algorithm for optimal sensor placement in structural health monitoring. *Measur. Sci. Technol.* 26 (6), 065104.
- Jiang, R., Wu, Q.S., Zhu, Z.J., 2001. Full velocity difference model for a car-following theory. *Phys. Rev. E* 64 (1), 017101.
- Jiang, R., Wu, Q.S., Zhu, Z.J., 2002. A new continuum model for traffic flow and numerical tests. *Transp. Res. Part B* 36, 405–419.
- Jin, J., Ran, B., 2011. Empirical Characteristics of Vehicular (Lagrangian) Fundamental Diagrams and Shock Waves. In: *Transportation Research Board 90th Annual Meeting*, Paper 114058, Washington, DC.
- Kim, T., Zhang, H., 2004. An empirical study on gap time and its relation to the fundamental diagram of traffic flow. In: *Proceedings of the 7th International IEEE Conference on Intelligent Transportation Systems*. IEEE, Washington, DC, pp. 94–99.
- Kim, T., Zhang, H., 2008. A stochastic wave propagation model. *Transp. Res. Part B* 42 (7), 619–634.
- Koshi, M., Iwasaki, M., Ohkura, I., 1983. Some findings and an overview on vehicular flow characteristics. In: Hurdle, V.F., Hauer, E., Stewart, G.N. (Eds.), *8th International Symposium on Transportation and Traffic Flow Theory*. University of Toronto Press, Toronto, pp. 403–426.
- Laval, J., Leclercq, L., 2013. The Hamilton-Jacobi partial differential equation and the three representations of traffic flow. *Transp. Res. Part B* 52, 17–30.
- Leclercq, L., Laval, J., Chevallier, E., 2007. The Lagrangian coordinate system and what it means for first order traffic flow models. In: Heydecker, B., Bell, M., Allsop, R. (Eds.), *17th International Symposium on Transportation and Traffic Theory*. Elsevier, New York.
- Lee, H.K., Lee, H.W., Kim, D., 2001. Macroscopic traffic models from microscopic car-following models. *Phys. Rev. E* 64 (5), 056126.
- Lighthill, M.J., Whitham, J.B., 1955. On kinematic waves II: a theory of traffic flow in long crowded roads. *Proc. Royal Soc. A* 229, 317–345.
- Liu, G.D., Lyrintzis, A.S., Michalopoulos, P.G., 1998. Improved high-order model for freeway traffic flow. *Transp. Res. Rec.* 1644, 37–46.
- Makigami, Y., Newell, G., Rothery, R., 1971. Three-dimensional representation of traffic flow. *Transp. Sci.* 5 (3), 302–313.
- Newell, G., 1961. Nonlinear effects in the dynamics of car following. *Oper. Res.* 9 (2), 209–229.
- Ni, D., Leonard, J., Jia, C., Wang, J., 2015. Vehicle longitudinal control and traffic stream modeling. *Transp. Sci. Articles Adv.*, 1–16.
- Pipes, L., 1965. Wave theories of traffic flow. *J. Franklin Inst.* 280 (1), 23–41.
- Pipes, L., 1967. Car following models and the fundamental diagram of road traffic. *Transp. Res.* 1 (1), 21–29.
- Rakha, H., Arafeh, M., 2010. Calibrating steady-state traffic stream and car-following models using loop detector data. *Transp. Sci.* 44 (2), 151–168.
- Rankine, W.J.M., 1870. On the thermodynamic theory of waves of finite longitudinal disturbances. *Philos. Trans. Royal Soc. London* 160, 277–288.
- Richards, P.I., 1956. Shockwaves on the highway. *Oper. Res.* 4, 42–51.
- Smulders, S., 1990. Control of freeway traffic flow by variable speed signs. *Transp. Res. Part B* 24 (2), 111–132.
- Tang, T.Q., Huang, H.J., Zhao, S.G., Shang, H.Y., 2009. A new dynamic model for heterogeneous traffic flow. *Phys. Lett. A* 373, 2461–2466.
- Treiber, M., Hennecke, A., Helbing, D., 2000. Congested traffic states in empirical observations and microscopic simulations. *Phys. Rev. E* 62, 1805–1824.
- Treiber, M., Kesting, A., 2013. *Traffic Flow Dynamics: Data, Models and Simulation*. Springer.
- Underwood, R.T., 1961. *Speed, Volume, and Density Relationship. Quality and Theory of Traffic Flow Report*. Yale University, New Haven, CT, pp. 141–188.
- Van Aerde, M., 1995. Single regime speed-flow-density relationship for congested and uncongested highways. In: *Transportation Research Board 74th Annual Meeting*, Paper 950802, Washington, DC.
- Yi, T.H., Zhou, G.D., Li, H.N., Zhang, X.D., 2015. Optimal sensor placement for health monitoring of high-rise structure based on collaborative-climb monkey algorithm. *Struct. Eng. Mech.* 54 (2), 305–317.
- Yuan, Y.F., 2013. *Lagrangian multi-class traffic state estimation Ph.D. Thesis*. Delft University of Technology, Netherlands.
- Zhang, H.M., 2002. A non equilibrium traffic model devoid of gas-like behavior. *Transp. Res. Part B* 36, 275–290.
- Zhang, H., Kim, T., 2005. A car-following theory for multiphase vehicular traffic flow. *Transp. Res. Part B* 39 (5), 385–399.
- Zhao, R.Q., Tang, W.S., 2008. Monkey algorithm for global numerical optimization. *J. Uncertain Syst.* 2 (3), 165–176.
- Zheng, L., 2013. An improved monkey algorithm with dynamic adaptation. *Appl. Math. Comput.* 222, 645–657.
- Zheng, L., Jin, J., Huang, H., 2015. An anisotropic continuum model considering bi-directional information impact. *Transp. Res. Part B* 75, 36–57.
- Zhou, X., Lü, Y., 2011. A novel macroscopic traffic model based on generalized optimal velocity model. *Chinese Phys. B* 20 (1), 014501.